Available online at www.sciencedirect.com
ScienceDirect
Geochimica et Cosmochimica Acta 74 (2010) 7307–7328
Geochimica et Cosmochimica Acta
www.elsevier.com/locate/gca

# Trace element systematics and $^{147}Sm$–$^{143}Nd$ and $^{176}Lu$–$^{176}Hf$ ages of Larkman Nunatak 06319: Closed-system fractional crystallization of an enriched shergottite magma

J.T. Shafer [a,b,*], A.D. Brandon [a,c], T.J. Lapen [a], M. Righter [a], A.H. Peslier [d], B.L. Beard [e,f]

[a] Department of Earth and Atmospheric Sciences, University of Houston, Houston, TX 77204, USA
[b] Lunar and Planetary Institute, Houston, TX 77059, USA
[c] ARES, NASA Johnson Space Center, Houston, TX 77058, USA
[d] Jacobs Technology, ESCG, Mail Code JE23, Houston, TX 77058, USA
[e] Department of Geosciences, University of Wisconsin-Madison, Madison, WI 53706, USA
[f] NASA Astrobiology Institute, USA

Received 30 March 2010; accepted in revised form 7 September 2010; available online 17 September 2010

**Abstract**

Combined $^{147}Sm$–$^{143}Nd$ and $^{176}Lu$–$^{176}Hf$ chronology of the martian meteorite Larkman Nunatak (LAR) 06319 indicates an igneous crystallization age of 193 ± 20 Ma (2$\sigma$ weighted mean). The individual $^{147}Sm$–$^{143}Nd$ and $^{176}Lu$–$^{176}Hf$ internal isochron ages are 183 ± 12 Ma and 197 ± 29 Ma, respectively, and are concordant with two previously determined $^{147}Sm$–$^{143}Nd$ and $^{87}Rb$–$^{87}Sr$ internal isochron ages of 190 ± 26 Ma and 207 ± 14 Ma, respectively (Shih et al., 2009). With respect to the $^{147}Sm$–$^{143}Nd$ isotope systematics, maskelynite lies above the isochron defined by primary igneous phases and is therefore not in isotopic equilibrium with the other phases in the rock. Non-isochronous maskelynite is interpreted to result from shock-induced reaction between plagioclase and partial melts of pyroxene and phosphate during transformation to maskelynite, which resulted in it having unsupported $^{143}Nd$ relative to its measured $^{147}Sm/^{144}Nd$ ratio. The rare earth element (REE) and high field strength element (HFSE) compositions of major constituent minerals can be modeled as the result of progressive crystallization of a single magma with no addition of secondary components. The concordant ages, combined with igneous textures, mineralogy, and trace element systematics indicate that the weighted average of the radiometric ages records the true crystallization age of this rock. The young igneous age for LAR 06319 and other shergottites are in conflict with models that advocate for circa 4.1 Ga crystallization ages of shergottites from Pb isotope compositions, however, they are consistent with updated crater counting statistics indicating that young volcanic activity on Mars is more widespread than previously realized (Neukum et al., 2010).
© 2010 Elsevier Ltd. All rights reserved.

## 1. INTRODUCTION

There is considerable debate regarding the igneous ages of shergottite meteorites. Young (~150–575 Ma) $^{147}Sm$–$^{143}Nd$ and $^{176}Lu$–$^{176}Hf$ internal isochron ages in shergottites are in contrast to the purported ancient (>4.0 Ga) $^{206}Pb$–$^{207}Pb$ ages of many of these same rocks (Borg et al., 1997, 2002, 2003, 2005; Brandon et al., 2004; Bouvier et al., 2005, 2008, 2009; Debaille et al., 2008; Lapen et al., 2008, 2009; Symes et al., 2008; Walton et al., 2008; Nyquist et al., 2009; Shih et al., 2009). The young ages have been interpreted to result from resetting by much later events such as fluid–rock interaction or shock (Bouvier et al., 2005, 2008, 2009), while the

* Corresponding author at: Department of Earth and Atmospheric Sciences, University of Houston, Houston, TX 77204, USA. Tel.: +1 713 677 3404; fax: +1 713 743 7906.
*E-mail address:* jtshafer@uh.edu (J.T. Shafer).

0016-7037/$ - see front matter © 2010 Elsevier Ltd. All rights reserved.
doi:10.1016/j.gca.2010.09.009

ancient $^{207}Pb$–$^{206}Pb$ ages have been argued to be the result of terrestrial contamination or represent source closure ages (Jagoutz, 1991; Borg et al., 2005; Gaffney et al., 2007). Thus it remains unclear which of these age groups record the true magmatic ages of shergottites and whether the younger ages reflect post-crystallization resetting.

The meteorite LAR 06319 presents a unique opportunity to evaluate some of the mechanisms proposed to cause chronometric resetting in shergottites. Systematic petrological studies (Basu Sarbadhikari et al., 2009; Peslier et al., 2010) of LAR 06319 indicate that the phenocryst phases in this rock, unlike many shergottites (e.g., Shergotty, EETA79001 lithology A, Zagami), have major and trace element compositions that can be explained by fractional crystallization of the phenocryst assemblage. This is consistent with LAR 06319 representing a closed-system igneous process. The trace element compositions of LAR 06319 show it is a member of the enriched shergottite subgroup whose composition approximates that of a parental melt (Basu Sarbadhikari et al., 2009; Peslier et al., 2010). Hence, the relatively straightforward petrology and the apparent lack of aqueous alteration of LAR 06319 (Basu Sarbadhikari et al., 2009; Peslier et al., 2010), makes this rock an ideal candidate to examine coupled isotopic and trace element variations of an apparently near pristine enriched shergottite parental melt. Furthermore, preliminary $^{87}Rb$–$^{87}Sr$ and $^{147}Sm$–$^{143}Nd$ data give young internal isochron ages (Shih et al., 2009). This study of LAR 06319 presents new $^{147}Sm$–$^{143}Nd$ and $^{176}Lu$–$^{176}Hf$ isotopic data coupled with in-situ trace element concentrations on mineral phases in order to assess whether isotopic as well as major and trace element systematics result from igneous paragenesis or are a consequence of metamorphic equilibration associated with shock and/or fluid infiltration. This examination of LAR 06319 is a test of the hypothesis proposed by Bouvier et al. (2005, 2008, 2009) that measured $^{87}Rb$–$^{87}Sr$, $^{147}Sm$–$^{143}Nd$, and $^{176}Lu$–$^{176}Hf$ ages are reset to <575 Ma.

## 2. PETROGRAPHY

Detailed petrography of LAR 06319 is presented elsewhere (Basu Sarbadhikari et al., 2009; Peslier et al., 2010). LAR 06319 is an olivine-phyric shergottite consisting of olivine megacrysts (up to 3 mm diameter) set in a matrix of olivine, pyroxene, and maskelynite interspersed with minor oxide phases, phosphate phases, and shock melt pockets (Basu Sarbadhikari et al., 2009; Peslier et al., 2010). Modal abundances for olivine, orthopyroxene, pigeonite, augite, maskelynite, and the minor phases are as follows, respectively: 24:4:28:22:18:4 vol% (Basu Sarbadhikari et al., 2009). The rock is extremely fresh, with no observed weathering products (Basu Sarbadhikari et al., 2009). Additionally, LAR 06319 is an Antarctic "cold desert" meteorite, the likes of which have been shown to generally suffer less alteration than hot desert finds (Crozaz and Wadhwa, 2001).

Olivine is typically brown to reddish-brown and often contains inclusions of oxide phases, pyroxene, and maskelynite. Melt inclusions within the cores of the olivine megacrysts have trace element compositions that are similar to that of the bulk rock (Basu Sarbadhikari et al., 2009). The olivine megacrysts have been interpreted as phenocrysts, rather than xenocrysts that are common in other olivine-phyric shergottites (Barrat et al., 2002; Basu Sarbadhikari et al., 2009; Peslier et al., 2010). Olivine in equilibrium with the bulk rock would have $Fo_{81}$ (% forsterite content), comparable to the measured $Fo_{77}$ of the most magnesian olivine (Basu Sarbadhikari et al., 2009). In addition, the olivine megacrysts are strongly zoned from core-to-rim, unlike xenocrystic olivine from NWA 1068 (Barrat et al., 2002; Basu Sarbadhikari et al., 2009). This evidence suggests that the olivine megacrysts formed early in magma conduits and eventually became entrained during the ascent of the magma in which they crystallized. The cores of the olivine megacrysts are typically more magnesian than the rims ($Fo_{76}$ vs. $Fo_{60}$), while groundmass olivine crystals are not zoned and are more Fe-rich ($Fo_{50}$) (Peslier et al., 2010). The MgO/FeO ratios of liquids in equilibrium with the olivine megacryst cores are 0.51–0.59 (Peslier et al., 2010), while the rims are in equilibrium with a liquid with a MgO/FeO ratio of 0.29–0.50 (Peslier et al., 2010). These liquids are too MgO-rich to be in equilibrium with the groundmass olivine, which indicate equilibrium liquid MgO/FeO ratios of 0.18–0.20 (Peslier et al., 2010). Thus, the major element data show that the olivine megacrysts grew in an initially MgO-rich liquid that became progressively Fe-rich, indicating that the groundmass olivine did not crystallize concurrently with the megacryst olivine (Peslier et al., 2010).

Pyroxene is common in LAR 06319 and consists primarily of pigeonite. Large (up to 3 mm long) pyroxene laths are present throughout the section, typically with Mg-rich ($En_{70}Fs_{25}Wo_5$, Mg# = 75) cores rimmed with calcic ($En_{50}Fs_{25}Wo_{25}$, Mg# = 60–65) and Fe-rich compositions ($En_{45}Fs_{45}Wo_{10}$, Mg# = 50). Smaller groundmass pyroxenes are typically more Fe-rich than the larger phenocrystic pyroxene (Peslier et al., 2010).

Like most olivine-phyric shergottites, LAR 06319 shows evidence of experiencing moderate shock pressures of ~30–35 GPa (Basu Sarbadhikari et al., 2009). Shock features in LAR 06319 include maskelynite (shock-disordered plagioclase, $An_{52}Ab_{45}$ (Peslier et al., 2010)) that is typically interstitial. Occasionally maskelynite is present as elongate laths 1–1.5 mm long with aspect ratios of 10–20. Significantly, all plagioclase has been converted into maskelynite and there are distinct melt pockets in our thick section as well as melt veins cutting through other sections (Basu Sarbadhikari et al., 2009). Extensive fracturing of olivine megacrysts is also related to shock.

Overall, the bulk composition of LAR 06319 approximates a melt that could be parental to the basaltic shergottites and is thus an important sample for constraining their evolution (Basu Sarbadhikari et al., 2009; Peslier et al., 2010).

## 3. ANALYTICAL TECHNIQUES

An ~800 mg aliquot of LAR 06319,15 was crushed in an alumina mortar and pestle used exclusively for martian meteorites. The mortar and pestle were pre-cleaned by repeatedly grinding Ottawa quartz sand in ethanol. The crushed material was sieved into >325 mesh (44 μm or less),

200–325 mesh (44–75 μm), 100–200 mesh (75–150 μm), and <100 mesh (greater than 152 μm) size fractions using Teflon sieve rings with replaceable mesh. The entire sieve stack was rinsed in ethanol and cleaned prior to using. Each size fraction was weighed and stored for further processing. The 200–325 mesh fraction was separated using heavy liquids. Methylene iodide ($p = 3.3$ g/cm$^3$) was used to separate maskelynite from pyroxene and olivine. Clerici's Solution (thallium malonate, $p = 3.55$ g/cm$^3$) was then used to separate pyroxene from olivine. Finally, olivine was purified from the remaining heavy material (mostly oxides) using a 4.05 g/cm$^3$ Clerici's Solution. All separates using heavy liquids were thoroughly washed using acetone (for the methylene iodide separates) and 18 MΩ $H_2O$ (for the Clerici's Solution separates) and visually inspected to ensure the proper separation of the phases. All phases separated by heavy liquids are referred to with the prefix "HL" followed by the name of the phase.

The 100–200 mesh fraction was purified by using a Frantz magnetic separator in 0.1 A intervals starting at 0.1 A. Each non-magnetic fraction was re-processed until no further magnetic material was produced. From this, maskelynite, pyroxene, and olivine fractions were isolated and further purified by handpicking. Hybrid crystals containing two or more phases were common due to the relatively small grain size of the groundmass. Crystals composed primarily of maskelynite but containing visible inclusions or intergrowths of other primary phases were designated hybrid-maskelynite. Due to the various phases present as inclusions or intergrowths and the proportion of the contaminant phase to maskelynite, these hybrid crystals were present throughout all of the Frantz magnetic separates, which were then hand-picked and collected as a distinct cut. A similar procedure was performed for crystals composed primarily of pyroxene but containing inclusions or intergrowths of other primary phases. In almost all cases for the reject maskelynite and pyroxene, the contaminating phases were either pyroxene or maskelynite, respectively, with oxide and phosphate being minor contaminants. Olivine generally formed distinct and relatively pure crystal fragments due to the abundance of the olivine megacrysts and groundmass olivine. While olivine fragments containing obvious inclusions were rejected, the dark color of the olivine crystals made unambiguous identification of pure crystals difficult. The reject cuts containing hybrid crystals are referred to with the prefix "H" followed by the name of the dominant phase. Purified cuts are referred to simply by the name of the phase.

This mineral separation procedure resulted in the following cuts: >325 mesh fraction (BR, fines assumed to approximate the bulk rock); 200–325 mesh maskelynite-rich (HL-MASK), pyroxene-rich (HL-PYX), olivine-rich, and oxide-rich fractions; and 100–200 mesh maskelynite (MASK), hybrid-maskelynite (H-MASK), pyroxene (PYX), hybrid-pyroxene (H-PYX), and olivine (OL). The close similarity in Sm, Nd, Lu, and Hf concentrations measured by isotope dilution in sample BR U (Table 3) to the bulk rock chemical composition of LAR 06319 (Basu Sarbadhikari et al., 2009) suggests that the fines are a close approximation of the bulk rock composition.

The bulk rock and mineral separate fractions were processed in four dissolution/analysis campaigns. Fractions from the 1st campaign were analyzed for both $^{176}$Lu–$^{176}$Hf and $^{147}$Sm–$^{143}$Nd isotopes. Samples from subsequent campaigns were analyzed only for $^{147}$Sm–$^{143}$Nd. Table 1 has descriptions of each sample and the corresponding abbreviated name that will be used throughout the rest of the text.

Unleached bulk rock and mineral separates were ultrasonicated in cold acetic acid for 10 min in order to remove any potential surface contaminants. The acetic acid supernatant for each unleached sample was reserved and combined into a single aliquot. Leached samples were ultrasonicated in cold 0.1 N or 2 N HCl for 10 min. In each case, the supernatant leachate was decanted from the residues and reserved for analysis. The residues were subsequently washed three times with ultrapure $H_2O$, which was added to the reserved leachate. The residues were then oven dried and reweighed prior to dissolution. The leachates were taken to dryness on a hotplate. The general dissolution scheme is as follows: hotplate digestion in 29 M HF to facilitate the majority of silicate breakdown, Lu–Hf and Sm–Nd spiking and Parr digestion vessel dissolution in 4:1 HF:$HNO_3$ to dissolve the remaining minerals, acidification with 12 N HCl, Parr digestion vessel dissolution in 8 N HCl, addition of perchloric acid to remove insoluble fluorides, and repeated acidifications with 6 M HCl until solutions were clear. In between each step, the sample solutions were taken to dryness, generally at 50 °C. The Parr digestion vessels were not used for leachate samples although the same acids and proportions were used for all samples. Following the final dry down, the samples were reacidified in 2.5 N HCl for column chemistry.

Samarium, Nd, Lu, and Hf were purified using a four-column procedure beginning with Fe removal via an anion exchange (AG1X8 200–400 mesh resin) and HCl, then isolation of Hf using Eichrom Ln-spec resin, followed by isolation of the REE via cation exchange (AG50W-X8 200–400 mesh resin), and concluding with isolation of Lu, Sm, and Nd (AG50W-X4 200–400 mesh resin in $NH_4$ form with α-HIBA). A two-column procedure (REE isolation via cation exchange and Sm–Nd purification using α-HIBA) was performed for samples analyzed for only $^{147}$Sm–$^{143}$Nd (Lapen et al., 2004, 2005).

Samarium and Nd concentrations were measured via isotope dilution at NASA, Johnson Space Center using a ThermoFinnigan *Triton* thermal ionization mass spectrometer (TIMS). Neodymium was loaded on a single filament in 2 N HCl and covered with a slurry of 5% $H_3PO_4$ and tantalum oxide activator (Harvey and Baxter, 2009). Neodymium isotopic ratios were measured as oxides in static mode and corrected offline for oxide interferences and instrumental mass bias using $^{146}$Nd/$^{144}$Nd = 0.7219 and an exponential mass fractionation law. Samarium was loaded on double filaments with $H_3PO_4$ as an activator and run as a metal using $^{147}$Sm/$^{152}$Sm = 0.56081 to correct for instrumental mass bias. NdO isobaric interferences were corrected using $^{17}$O/$^{16}$O = 0.000393 and $^{18}$O/$^{16}$O = 0.002052. Procedural blanks were run for each set of dissolutions. Sm and Nd averaged 33 and 67 pg, respectively, which contributed negligibly to the measured ratios. Replicate

Table 1
LAR 06319 sample descriptions and weights.

| Sample name | Processing notes | Dissolution notes | Sample wt. (g) | $^{176}Lu$–$^{176}Hf$ | $^{147}Sm$–$^{143}Nd$ |
|---|---|---|---|---|---|
| BR U | >325 mesh bulk rock | Acetic washed | 0.01924 | × | × |
| BR 01N R | >325 mesh bulk rock | 0.1 N HCl residue | 0.01785 | × | |
| BR 01N L | >325 mesh bulk rock | 0.1 N HCl leachate | 0.00144 | | × |
| BR 2N R-1st | >325 mesh bulk rock | 2 N HCl residue | 0.01520 | × | |
| BR 2N L-1st | >325 mesh bulk rock | 2 N HCl leachate | 0.00265 | | × |
| PYX U | Pyroxene, magnetically separated, hand-picked | Acetic washed | 0.06678 | × | × |
| HMASK U | Maskelynite, magnetically separated, hand-picked rejects | Acetic washed | 0.03196 | × | × |
| OL U | Olivine, magnetically separated, hand-picked | Acetic washed | 0.04874 | | × |
| HL-PYX 2N R | Pyroxene, heavy liquid separated | 2 N HCl residue | 0.04307 | | × |
| HL-PYX 2N L | Pyroxene, heavy liquid separated | 2 N HCl leachate | 0.00190 | | × |
| BR 2N R-3rd | >325 mesh bulk rock | 2 N HCl residue | 0.02662 | | × |
| H-PYX 2N R | Pyroxene, magnetically separated, hand-picked rejects | 2 N HCl residue | 0.03204 | | × |
| H-PYX 2N L | Pyroxene, magnetically separated, hand-picked rejects | 2 N HCl leachate | 0.00259 | | × |
| BR 2N R-4th | >325 mesh bulk rock | 2 N HCl residue | 0.02030 | | × |
| BR 2N L-4th | >325 mesh bulk rock | 2 N HCl leachate | 0.00679 | | × |
| HMASK 2N R | Maskelynite, magnetically separated, hand-picked rejects | 2 N HCl residue | 0.02236 | | × |
| HMASK 2N L | Maskelynite, magnetically separated, hand-picked rejects | 2 N HCl leachate | 0.00399 | | × |
| HL-MASK 2N R | Maskelynite, heavy liquid separated | 2 N HCl residue | 0.02540 | | × |
| HL-MASK 2N L | Maskelynite, heavy liquid separated | 2 N HCl leachate | 0.00348 | | × |

analyses of 4 ng Ames Nd standard yielded an external precision ($2\sigma$) of 0.000010 (~20 ppm) on the $^{143}Nd/^{144}Nd$ ratio. Replicate analyses of La Jolla yielded an average $^{143}Nd/^{144}Nd$ ratio of $0.511847 \pm 0.000006$.

Lutetium and Hf were analyzed using a GV Instruments *IsoProbe* MC–ICP-MS at the University of Wisconsin-Madison using procedures outlined elsewhere (Lapen et al., 2004, 2010). During Hf isotope analysis, the following isotopes were analyzed: $^{176}Hf$, $^{177}Hf$, $^{178}Hf$, $^{179}Hf$, and $^{180}Hf$ as well as $^{173}Yb$, $^{175}Lu$, and $^{182}W$, which were used to correct for isobaric interferences on $^{176}Hf$ (Yb and Lu) and $^{180}Hf$ (W). The $^{181}Ta$ isotopes were not monitored for isobaric $^{180}Ta$ interference on $^{180}Hf$ because the concentration of Ta in the Hf cuts is insignificant. Instrumental mass fractionation correction and spike striping followed methods of Lapen et al. (2004). Standards and samples were measured in solutions of 5–30 ppb and were introduced into the mass spectrometer through an Aridus II desolvating nebulizer fitted with a 50 μl/min self-aspirating nebulizer. Total procedural blanks for Hf and Lu were <80 pg. Throughout the hafnium isotope analysis of samples, the UW-AMES Hf standard was used to correct for instrumental fractionation. JMC-475 Hf was analyzed as an unknown standard. Repeated analysis of the Hf standard JMC-475 yielded $^{176}Hf/^{177}Hf = 0.282162 \pm 11$ (2 SD, $n = 25$). Lutetium isotope analyses followed procedures in Lapen et al. (2004). External reproducibility in $^{176}Hf/^{177}Hf$ and $^{176}Lu/^{177}Hf$ ratios are 0.005% and 0.2% ($2\sigma$), respectively, and these values are used as the measurement uncertainty for the age calculations.

Trace element abundances were measure by laser ablation inductively coupled plasma-mass spectrometry (LA-ICP-MS) of single spots on a thick section of LAR 06319 at the University of Houston using a CETAC LSX-213 laser ablation system connected to a Varian 810-MS quadrupole ICP-MS. A He carrier gas was used to enhance transport efficiency of ablated material. For each analyzed spot (20–100 μm in diameter), we measured a 10–15 s gas blank prior to sample ablation. Samples were ablated for 20–30 s at a laser power of ~3 mJ/4 ns pulse, repetition rate of 20 Hz, and 213 nm wavelength. All trace element data were corrected for laser and ICP-MS elemental fractionation with internal elements Si, Mg, and Cr calibrated by EPMA and the USGS external standard BHVO-2G glass using the commercial data reduction software package Glitter. The USGS SRM BIR-1G glass standard was used to monitor external reproducibility and instrument drift.

## 4. DISCUSSION

### 4.1. In-situ trace element concentrations

Representative trace element concentrations of the major silicate phases, melt inclusions, and phosphate are presented in Table 2. Chondrite normalized incompatible trace element profiles of these phases are shown in Fig. 1. These new results are very similar to those found in Basu Sarbadhikari et al. (2009).

Average compatible element (Cr, Ni, Cu, V) concentrations are elevated in the cores of the large olivine megacrysts

Table 2
LAR 06319 laser ablation ICP-MS representative compositions of primary phases.

| | Olivine megacryst core | | | Olivine megacryst rim | | | Olivine groundmass | | | High-P maskelynite | Low-P maskelynite | | |
|---|---|---|---|---|---|---|---|---|---|---|---|---|---|
| | Min | Max | Median | Min | Max | Median | Min | Max | Median | | Min | Max | Median |
| Number | | | 18 | | | 8 | | | 17 | 1 | | | 8 |
| $P_2O_5$ (wt%) | 0.01 | 0.03 | 0.02 | 0.01 | 0.05 | 0.02 | 0.01 | 0.22 | 0.04 | 2.04 | 0.02 | 0.08 | 0.05 |
| Sc (ppm) | 6.47 | 8.65 | 7.42 | 6.82 | 8.29 | 7.95 | 7.80 | 13.6 | 8.80 | 67.7 | 0.62 | 66.8 | 17.4 |
| V | 25.2 | *76.2* | 33.2 | 25.2 | *36.8* | 31.0 | 7.51 | *130* | 22.9 | *1179* | 5.01 | 345 | 66.0 |
| Cr | 798 | *4381* | 1225 | 905 | *1234* | 1108 | 60 | *8123* | 707 | *13963* | 20.6 | *1879* | 184 |
| Co | 102 | 115 | 108 | 96.9 | 111 | 103 | 87 | 100 | 94 | 56 | 0.54 | 37.4 | 23.4 |
| Ni | 507 | 791 | 692 | 556 | 715 | 640 | 297 | 476 | 419 | 134 | 20.7 | 78.4 | 50.5 |
| Cu | 7.52 | 32.9 | 15.7 | 2.85 | 23.0 | 9.85 | 1.96 | 9.66 | 4.42 | 25.5 | 0.23 | 8.40 | 4.99 |
| Ga | 0.31 | 1.75 | 0.47 | 0.48 | 0.91 | 0.53 | 0.36 | 2.41 | 0.78 | 65.1 | 16.1 | 39.5 | 32.6 |
| Ge | <0.29 | 0.96 | 0.72 | 0.38 | 0.85 | 0.51 | 0.35 | 1.04 | 0.66 | 1.41 | 0.01 | 1.28 | 0.52 |
| Sr | <0.031 | 0.29 | 0.11 | <0.029 | 0.19 | <0.029 | <0.024 | 1.98 | 0.14 | 115 | 43.0 | 192 | 163 |
| Y | 0.12 | 0.33 | 0.18 | 0.09 | 0.26 | 0.15 | 0.11 | 0.73 | 0.19 | 98.2 | 0.23 | 8.86 | 4.03 |
| Zr | <0.36 | *1.62* | <0.36 | <0.34 | <0.34 | <0.34 | <0.31 | *2.37* | 0.56 | *1272* | 11.8 | 158 | 22.7 |
| Nb | <0.008 | 0.17 | 0.01 | <0.009 | 0.03 | <0.009 | 0.01 | 0.11 | 0.03 | 109 | 0.39 | 9.28 | 1.05 |
| Ba | <0.056 | 0.12 | <0.056 | <0.053 | 0.10 | 0.06 | <0.044 | 1.61 | 0.11 | 287 | 20.3 | 119 | 75.9 |
| La | <0.005 | 0.03 | 0.01 | <0.005 | 0.01 | <0.005 | <0.004 | 0.08 | 0.01 | 17.0 | 0.07 | 0.47 | 0.27 |
| Ce | <0.004 | 0.08 | 0.01 | <0.004 | 0.03 | 0.01 | 0.01 | 0.19 | 0.02 | 41.3 | 0.21 | 1.32 | 0.62 |
| Pr | <0.004 | 0.01 | <0.004 | <0.003 | 0.01 | <0.003 | <0.003 | 0.03 | 0.01 | 5.63 | 0.03 | 0.21 | 0.09 |
| Nd | <0.018 | 0.06 | <0.018 | <0.021 | 0.06 | <0.021 | <0.017 | 0.13 | 0.02 | 30.0 | 0.18 | 1.16 | 0.43 |
| Sm | <0.022 | 0.05 | <0.022 | <0.017 | 0.03 | <0.017 | <0.016 | 0.07 | <0.016 | 10.5 | 0.06 | 0.72 | 0.19 |
| Eu | <0.008 | <0.008 | <0.008 | <0.007 | 0.02 | <0.007 | <0.006 | 0.02 | <0.006 | 3.39 | 0.17 | 0.65 | 0.53 |
| Gd | <0.018 | 0.04 | <0.018 | <0.015 | 0.04 | <0.015 | <0.015 | 0.09 | 0.02 | 16.7 | 0.02 | 1.12 | 0.46 |
| Tb | <0.004 | 0.01 | <0.004 | <0.004 | 0.01 | <0.004 | <0.003 | 0.01 | 0.01 | 3.14 | 0.01 | 0.22 | 0.09 |
| Dy | <0.021 | 0.09 | <0.021 | <0.019 | 0.06 | 0.02 | <0.016 | 0.13 | 0.03 | 20.3 | 0.09 | 1.57 | 0.78 |
| Ho | <0.004 | 0.02 | 0.01 | <0.004 | 0.01 | 0.01 | <0.004 | 0.03 | 0.01 | 4.20 | 0.01 | 0.32 | 0.17 |
| Er | <0.017 | 0.05 | 0.03 | <0.019 | 0.06 | 0.02 | <0.013 | 0.11 | 0.04 | 11.7 | 0.03 | 1.07 | 0.52 |
| Tm | <0.003 | 0.01 | 0.01 | <0.004 | 0.02 | 0.001 | <0.003 | 0.02 | 0.01 | 1.60 | 0.01 | 0.14 | 0.08 |
| Yb | <0.015 | 0.09 | 0.04 | 0.03 | 0.08 | 0.05 | 0.03 | 0.15 | 0.09 | 10.3 | 0.06 | 1.00 | 0.47 |
| Lu | <0.004 | 0.02 | 0.01 | 0.01 | 0.01 | 0.01 | 0.01 | 0.04 | 0.02 | 1.44 | 0.01 | 0.16 | 0.07 |
| Hf | <0.016 | 0.08 | <0.016 | <0.015 | 0.06 | 0.02 | <0.013 | 0.07 | 0.02 | *38.7* | 0.40 | 3.58 | 0.73 |
| Ta | <0.005 | 0.01 | <0.005 | <0.006 | <0.006 | <0.006 | <0.004 | 0.01 | <0.004 | 3.93 | 0.01 | 0.36 | 0.05 |
| Th | <0.007 | 0.02 | <0.007 | <0.006 | 0.01 | <0.006 | <0.005 | 0.01 | <0.005 | 2.84 | 0.02 | 0.12 | 0.06 |
| U | <0.005 | 0.01 | <0.005 | <0.005 | 0.02 | 0.01 | <0.004 | 0.01 | <0.004 | 0.34 | 0.01 | 0.26 | 0.03 |

| | Pigeonite core | | | Pigeonite rim | | | Augite | | | Orthopyroxene | | |
|---|---|---|---|---|---|---|---|---|---|---|---|---|
| | Min | Max | Median | Min | Max | Median | Min | Max | Median | Min | Max | Median |
| Number | | | 4 | | | 7 | | | 3 | | | 3 |
| $P_2O_5$ (wt%) | 0.01 | 0.02 | 0.02 | 0.01 | 0.06 | 0.04 | 0.08 | 0.36 | 0.18 | 0.002 | 0.01 | 0.004 |
| Sc (ppm) | 29.1 | 37.5 | 32.7 | 48.1 | 108 | 61.1 | 34.3 | 62.2 | 44.1 | 17.4 | 25.6 | 19.9 |
| V | 148 | 227 | 198 | 274 | 621 | 359 | 109 | 458 | 185 | 108 | 166 | 120 |

(*continued on next page*)

Table 2 (*continued*)

| | Pigeonite core | | | Pigeonite rim | | | Augite | | | Orthopyroxene | | |
|---|---|---|---|---|---|---|---|---|---|---|---|---|
| | Min | Max | Median | Min | Max | Median | Min | Max | Median | Min | Max | Median |
| Number | | | 4 | | | 7 | | | 3 | | | 3 |
| Cr | 2138 | 2805 | 2560 | 2030 | 3555 | 2978 | 215 | *10315* | 741 | 2368 | 2872 | 2631 |
| Co | 46.3 | 50.5 | 48.4 | 40.1 | 49.0 | 44.9 | 35.4 | 108 | 48.3 | 50.2 | 52.9 | 50.7 |
| Ni | 184 | 190 | 189 | 100 | 177 | 146 | 47.3 | *315* | 88 | 188 | 214 | 190 |
| Cu | 5.44 | 16.4 | 13.7 | 10.17 | 15.9 | 11.4 | 7.32 | 12.1 | 9.71 | 5.50 | 7.06 | 6.03 |
| Ga | 1.63 | 2.31 | 1.88 | 3.95 | 7.46 | 4.30 | 9.62 | 19.8 | 17.9 | 1.03 | 1.34 | 1.17 |
| Ge | 0.42 | 0.75 | 0.64 | 0.74 | 1.19 | 0.92 | 1.00 | 1.49 | 1.16 | 0.66 | 1.07 | 0.84 |
| Sr | 0.79 | 1.27 | 1.03 | 2.89 | 9.55 | 4.87 | 14.5 | 49.7 | 17.1 | 0.09 | 0.15 | 0.15 |
| Y | 1.46 | 2.23 | 1.68 | 4.20 | 10.7 | 5.16 | 6.40 | 19.4 | 6.79 | 0.61 | 0.94 | 0.66 |
| Zr | 1.13 | 2.66 | 2.30 | 7.36 | 14.5 | 12.0 | 28.9 | 68.7 | 49.1 | 0.32 | 0.46 | 0.44 |
| Nb | 0.08 | 0.18 | 0.11 | 0.13 | 0.70 | 0.37 | 0.67 | 2.64 | 1.93 | 0.03 | 0.03 | 0.03 |
| Ba | 0.34 | 0.70 | 0.55 | 0.97 | 5.16 | 3.58 | 5.90 | 51.2 | 13.2 | <0.025 | <0.025 | <0.025 |
| La | 0.03 | 0.10 | 0.05 | 0.07 | 0.31 | 0.17 | 0.57 | 2.42 | 0.63 | 0.01 | 0.01 | 0.01 |
| Ce | 0.09 | 0.27 | 0.15 | 0.26 | 0.90 | 0.53 | 1.40 | 6.34 | 1.96 | 0.004 | 0.02 | 0.02 |
| Pr | 0.02 | 0.04 | 0.03 | 0.06 | 0.14 | 0.10 | 0.25 | 0.89 | 0.25 | <0.003 | <0.003 | <0.003 |
| Nd | 0.09 | 0.21 | 0.16 | 0.38 | 1.09 | 0.61 | 1.06 | 4.59 | 1.17 | <0.014 | 0.06 | 0.04 |
| Sm | 0.06 | 0.11 | 0.08 | 0.22 | 0.65 | 0.31 | 0.50 | 1.84 | 0.53 | <0.01 | 0.06 | 0.01 |
| Eu | 0.02 | 0.05 | 0.03 | 0.09 | 0.23 | 0.12 | 0.21 | 0.54 | 0.29 | 0.01 | 0.01 | 0.01 |
| Gd | 0.14 | 0.27 | 0.18 | 0.49 | 1.33 | 0.70 | 0.81 | 3.07 | 0.91 | 0.03 | 0.08 | 0.05 |
| Tb | 0.03 | 0.06 | 0.04 | 0.11 | 0.30 | 0.13 | 0.17 | 0.59 | 0.18 | 0.01 | 0.03 | 0.01 |
| Dy | 0.25 | 0.42 | 0.29 | 0.85 | 2.16 | 0.99 | 1.21 | 3.98 | 1.24 | 0.08 | 0.12 | 0.08 |
| Ho | 0.06 | 0.10 | 0.06 | 0.19 | 0.45 | 0.22 | 0.28 | 0.89 | 0.28 | 0.02 | 0.04 | 0.03 |
| Er | 0.18 | 0.30 | 0.22 | 0.59 | 1.31 | 0.68 | 0.83 | 2.37 | 0.90 | 0.07 | 0.14 | 0.09 |
| Tm | 0.03 | 0.05 | 0.03 | 0.08 | 0.16 | 0.09 | 0.13 | 0.31 | 0.13 | 0.01 | 0.02 | 0.02 |
| Yb | 0.22 | 0.30 | 0.26 | 0.55 | 1.22 | 0.66 | 0.85 | 2.11 | 0.91 | 0.07 | 0.16 | 0.11 |
| Lu | 0.03 | 0.05 | 0.04 | 0.09 | 0.18 | 0.09 | 0.13 | 0.34 | 0.16 | 0.02 | 0.03 | 0.02 |
| Hf | 0.05 | 0.11 | 0.08 | 0.33 | 0.61 | 0.39 | 1.05 | 2.33 | 1.80 | 0.02 | 0.02 | 0.02 |
| Ta | 0.00 | 0.05 | 0.01 | <0.007 | 0.04 | 0.02 | 0.04 | 0.20 | 0.14 | <0.003 | 0.004 | <0.003 |
| Th | <0.005 | 0.02 | 0.01 | <0.009 | 0.06 | 0.05 | 0.09 | 0.33 | 0.14 | <0.007 | <0.007 | <0.007 |
| U | <0.004 | 0.01 | <0.004 | <0.005 | 0.05 | 0.02 | 0.02 | 0.05 | 0.02 | <0.004 | <0.004 | <0.004 |

| | Merrillite | Melt inclusion in olivine Median | BIR-1G | 2$\sigma$ SD | Gao et al. (2002) | Meas./SRM |
|---|---|---|---|---|---|---|
| Number | 1 | 2 | 10 | | | |
| $P_2O_5$ (wt%) | 24.2 | 0.74 | | | | |
| Sc (ppm) | 85.3 | 35.4 | 42.8 | 4.3 | 41 | 1.0 |
| V | 175 | 171 | 324 | 23 | 338 | 1.0 |
| Cr | 45.6 | 574 | 391 | 9.9 | 403 | 1.0 |
| Co | 43.6 | 21.9 | 52.1 | 2.3 | 57 | 0.9 |
| Ni | 179 | 204 | 176 | 14 | 190 | 0.9 |
| Cu | 37.1 | 8.22 | 117 | 8.9 | 132 | 0.9 |
| Ga | 59.5 | 13.6 | 14.9 | 1.0 | 17 | 0.9 |
| Ge | 3.55 | 1.04 | 1.2 | 0.36 | | |
| Sr | 274 | 125 | 108 | 13 | 104 | 1.0 |
| Y | 1341 | 17.9 | 14.2 | 1.7 | 13.3 | 1.1 |
| Zr | 521 | 68.3 | 13.9 | 1.8 | 12.9 | 1.1 |
| Nb | 6.39 | 8.42 | 0.51 | 0.06 | 0.48 | 1.1 |
| Ba | 205 | 24.0 | 6.42 | 0.33 | 6.3 | 1.0 |
| La | 264 | 2.38 | 0.60 | 0.06 | 0.60 | 1.0 |
| Ce | 618 | 6.39 | 1.85 | 0.15 | 1.9 | 1.0 |
| Pr | 93.6 | 0.92 | 0.37 | 0.03 | 0.36 | 1.0 |
| Nd | 459 | 4.18 | 2.36 | 0.20 | 2.3 | 1.0 |
| Sm | 165 | 1.57 | 1.07 | 0.10 | 1.1 | 1.0 |
| Eu | 47.2 | 0.63 | 0.50 | 0.05 | 0.51 | 1.0 |
| Gd | 253 | 2.69 | 1.83 | 0.18 | 1.6 | 1.1 |
| Tb | 44.4 | 0.47 | 0.34 | 0.03 | 0.32 | 1.1 |
| Dy | 289 | 3.12 | 2.49 | 0.29 | 2.3 | 1.1 |
| Ho | 57.7 | 0.65 | 0.55 | 0.05 | 0.51 | 1.1 |
| Er | 158 | 1.94 | 1.66 | 0.20 | 1.5 | 1.1 |
| Tm | 20.1 | 0.26 | 0.24 | 0.01 | 0.22 | 1.1 |
| Yb | 121 | 1.83 | 1.61 | 0.12 | 1.5 | 1.1 |
| Lu | 16.5 | 0.25 | 0.24 | 0.02 | 0.23 | 1.1 |
| Hf | 18.2 | 1.99 | 0.56 | 0.05 | 0.53 | 1.1 |
| Ta | 1.01 | 0.34 | 0.03 | 0.004 | 0.03 | 1.1 |
| Th | 33.6 | 0.37 | 0.03 | 0.01 | 0.03 | 1.1 |
| U | 3.9 | 0.12 | 0.02 | 0.005 | 0.03 | 0.5 |

Values in italics are likely influenced by oxide inclusions.

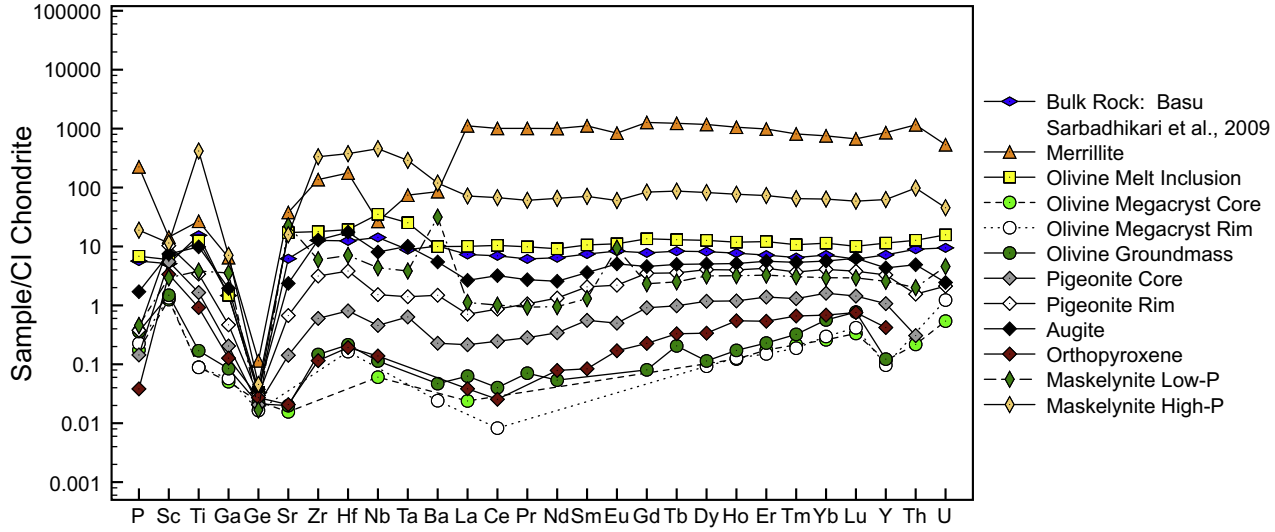


Fig. 1. In-situ incompatible trace element concentrations of the major phases in LAR 06319 normalized to C1 chondrite. Note that the low-P maskelynite has a LREE depleted profile and characteristic positive Eu anomaly while the high-P maskelynite has a generally flat REE profile and a subdued Eu anomaly. These characteristics indicate that the high-P maskelynite assimilated REE-enriched phosphate during the maskelynitization process (Basu Sarbadhikari et al., 2009). The REE pattern of the olivine melt inclusion is identical to the whole-rock REE profile of Basu Sarbadhikari et al. (2009).

compared to their rims, consistent with progressive crystallization in an evolving magma (Table 2). The smaller groundmass olivine crystals have similar to lower compatible element concentrations than the olivine megacryst rims (e.g., average groundmass olivine Ni = 419 ppm, Cu = 4.42 ppm, Co = 94 ppm, Cr = 707 ppm compared to average megacryst olivine rim Ni = 640 ppm, Cu = 9.85 ppm, Co = 103 ppm, Cr = 1108 ppm), indicating crystallization after that of the megacryst cores and rims in an evolving magma. Incompatible trace elements in the olivine crystals (both megacrysts and groundmass) are characteristically low, consistent with known partitioning behavior of these elements in olivine (Fig. 1). The olivine megacrysts contain melt inclusions whose REE patterns are subparallel to the bulk rock REE profile of Basu Sarbadhikari et al. (2009), i.e., essentially flat ($La/Yb_{CI} \sim 0.88$, CI subscript indicates normalization to CI chondrite (McDonough and Sun, 1995)) at ~10× chondritic (Fig. 1). The melt inclusions located in the most Mg-rich cores of the olivine megacrysts have been interpreted (Basu Sarbadhikari et al., 2009; Peslier et al., 2010) to be representative of the parent melt for LAR 06319.

Two compositional varieties of maskelynite are present based on their phosphorous contents: low-P and high-P. These distinct maskelynite compositions are noted in Basu Sarbadhikari et al. (2009) who suggest that the flat REE profile, reduced Eu anomaly ($Eu/Eu^* = 0.8$ in high-P maskelynite vs. 5.1 for low-P maskelynite), and generally higher REE (~100× chondritic vs. 2–5× chondritic) and $P_2O_5$ (~2 wt% vs. 0.05 wt%) concentrations in the high-P variety indicate assimilation of phosphate during maskelynitization (Fig. 1). The low-P maskelynite has LREE depleted profiles ($La/Yb_{CI} = 0.38$) similar to that in other shergottites as well as relatively high concentrations of elements strongly partitioned into the plagioclase crystal structure (e.g., $Ba_{CI} = 32$, $Eu_{CI} = 9.3$, and $Sr_{CI} = 22$) (Basu Sarbadhikari et al., 2009).

Pigeonite core and rim chondrite normalized incompatible trace element profiles are subparallel, although the pigeonite cores are slightly more LREE depleted than their rims ($La/Yb_{CI} = 0.13$ vs. 0.17, respectively). Overall trace element abundances are ~3× greater in the pigeonite rims than cores. Augite has higher incompatible trace element abundances and has a flatter overall chondrite normalized profile relative to pigeonite and orthopyroxene. Phosphate (merrillite) has the highest incompatible trace element concentrations at ~1000× chondritic.

The olivine-phyric shergottite LAR 06319 is more enriched in incompatible elements than most other olivine-phyric shergottites. Bulk rock incompatible trace element abundances of LAR 06319 are similar to that of NWA 1068 at ~10× chondritic (Barrat et al., 2002). This is at the lower range of basaltic shergottites (~8–20× chondritic), but higher than the other olivine-phyric and lherzolitic shergottites (~0.4–5× chondritic), which also tend to have LREE depleted normalized REE profiles (McSween et al., 1996; Rubin et al., 2000; Barrat et al., 2001, 2002; Jambon et al., 2002; Ikeda, 2004; Usui et al., 2008; Basu Sarbadhikari et al., 2009).

### 4.2. $^{147}Sm$–$^{143}Nd$ and $^{176}Lu$–$^{176}Hf$ ages and isotope systematics

#### 4.2.1. *$^{147}Sm$–$^{143}Nd$ age and systematics*

The $^{147}Sm$–$^{143}Nd$ age of LAR 06319 is 183 ± 12 Ma (MSWD = 2.2; ±2σ for all uncertainties listed hereon) based on a seven-point internal isochron (Table 3 and Fig. 2) with a derived initial $^{143}Nd/^{144}Nd$ isotope ratio of 0.512033 ± 0.000021 ($\varepsilon Nd_I = -7.21 \pm 0.41$ relative to CHUR). The isochron was calculated by the program Isoplot V3.7 (Ludwig,

Table 3
$^{143}Nd/^{144}Nd$ and $^{176}Hf/^{177}Hf$ data for LAR 06319.

| Sample | Sm (ppm) | Nd (ppm) | $^{147}Sm/^{144}Nd$[a] | $^{143}Nd/^{144}Nd$[b] | ±2 SD[c,e] | Lu (ppm) | Hf (ppm) | $^{176}Lu/^{177}Hf$[a] | $^{176}Hf/^{177}Hf$[d] | ±2 SD[e] |
|---|---|---|---|---|---|---|---|---|---|---|
| BR U | 1.12 | 2.87 | 0.2356 | 0.512307 | 4 | 0.20 | 1.60 | 0.0180 | 0.282216 | 10 |
| BR 01N R | | | | | | 0.078 | 1.75 | 0.0063 | 0.282158 | 8 |
| BR 01N L | 17.1 | 46.1 | 0.2229 | 0.512298 | 5 | | | | | |
| BR 2N R-1st | | | | | | 0.075 | 1.73 | 0.0062 | 0.282162 | 9 |
| BR 2N L-1st | 8.69 | 23.4 | 0.2233 | 0.512299 | 13 | | | | | |
| PYX U | 0.31 | 0.65 | 0.2896 | 0.512388 | 7 | 0.11 | 0.55 | 0.0294 | 0.282245 | 8 |
| HMASK U | 1.71 | 4.55 | 0.2273 | 0.512302 | 8 | 0.30 | 3.30 | 0.0127 | 0.282190 | 7 |
| OL U | 0.20 | 0.52 | 0.2324 | 0.512325 | 20 | | | | | |
| HL-PYX 2N R | 0.17 | 0.28 | 0.3533 | 0.512469 | 219 | | | | | |
| HL-PYX 2N L | 9.42 | 25.4 | 0.2230 | 0.512300 | 6 | | | | | |
| BR 2N R-3rd | 0.20 | 0.40 | 0.3050 | 0.512472 | 35 | | | | | |
| H-PYX 2N R | 0.23 | 0.37 | 0.3683 | 0.512474 | 8 | | | | | |
| H-PYX 2N L | 9.30 | 25.2 | 0.2226 | 0.512291 | 12 | | | | | |
| BR 2N R-4th | 0.23 | 0.38 | 0.3728 | 0.512453 | 27 | | | | | |
| BR 2N L-4th | 6.95 | 18.8 | 0.2230 | 0.512312 | 5 | | | | | |
| HMASK 2N R | 0.17 | 0.35 | 0.2947 | 0.512455 | 17 | | | | | |
| HMASK 2N L | 13.2 | 35.7 | 0.2227 | 0.512298 | 6 | | | | | |
| HL-MASK 2N R | 0.18 | 0.35 | 0.3080 | 0.512446 | 10 | | | | | |
| HL-MASK 2N L | 12.6 | 34.1 | 0.2229 | 0.512311 | 4 | | | | | |
| Acetic L | | | 0.2229 | 0.512301 | 7 | | | | | |
| Ames97 ($n = 20$) | | | | 0.512130 | 10 | | | | | |
| La Jolla ($n = 12$) | | | | 0.511847 | 6 | | | | | |

Sm and Nd concentrations determined by isotope dilution on ThermoFinnigan *Triton* TIMS at Johnson Space Center, NASA.
Lu and Hf concentrations determined by MC–ICP-MS at the University of Wisconsin.
[a] Errors on $^{147}Sm/^{144}Nd$ and $^{176}Lu/^{176}Hf$ are estimated to be 0.2%.
[b] Nd isotopic ratios were measured on ThermoFinnigan *Triton* TIMS at Johnson Space Center, NASA and were corrected to La Jolla 0.511858.
[c] Internal measured precision. A lower limit of the precision was set at 20 ppm in determining the isochron based on standard Ames97 external reproducibility.
[d] Hf isotopic ratios were measured on GV Instruments *IsoProbe* MC–ICP-MS at the University of Wisconsin.
[e] Errors apply to the last significant digits of the measured ratio.

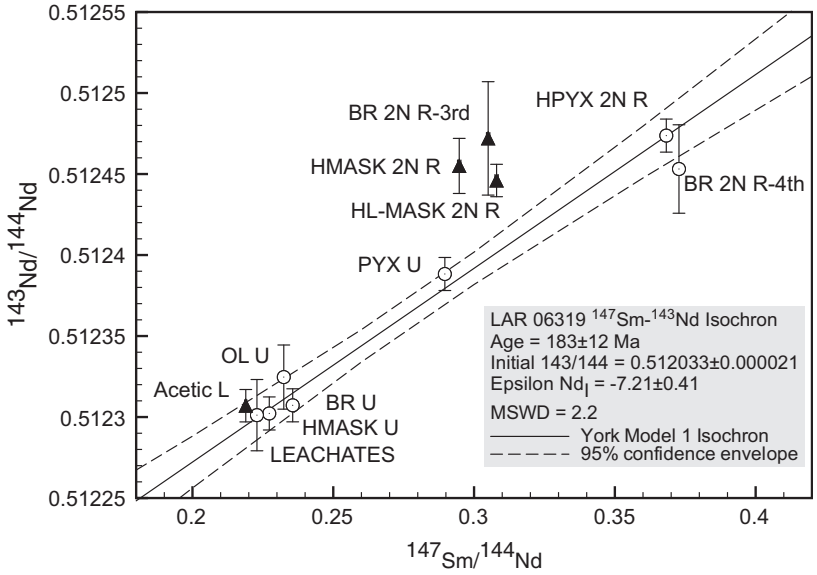


Fig. 2. Internal mineral $^{147}Sm$–$^{143}Nd$ isochron for LAR 06319. The $^{147}Sm$–$^{143}Nd$ age is $183 \pm 12$ Ma with an initial $^{143}Nd/^{144}Nd$ ratio of $0.512033 \pm 21$ ($-7.21$ $\varepsilon Nd_I$ relative to CHUR; present day $^{143}Nd^{144}Nd = 0.512638$, $^{147}Sm/^{144}Nd = 0.1967$, $^{147}Sm$ decay constant $= 6.54 \times 10^{-12}$ yr$^{-1}$). The program Isoplot V3.7 was used to generate a Model 1 isochron (i.e., all points used to define isochron are within expected geologic scatter) with a MSWD of 2.2. The multiple leachate samples were averaged and this single average leachate composition was used for the isochron. Samples BR 2N R-3rd, HL-MASK 2N R, HMASK 2N R, and Acetic L (solid black triangles) were not used as part of the isochron for reasons outlined in the text.

2003) using York's (1966) algorithm (Model 1 fit). This age is within error of the $^{147}Sm$–$^{143}Nd$ age for an internal isochron obtained by Shih et al. (2009) ($190 \pm 26$ Ma). The HCl leachates cluster at $^{143}Nd/^{144}Nd = 0.512301 \pm 0.000022$ and $^{147}Sm/^{144}Nd = 0.2234 \pm 0.0012$ and are the most unradiogenic fractions analyzed (Table 3 and Fig. 2). Because of their reproducibility for $^{143}Nd/^{144}Nd$ and $^{147}Sm/^{144}Nd$ ratios, the HCl leachates were averaged and treated as a single point for determining the isochron of LAR 06319. The error on the average leachate point was calculated by taking the square root of the summed squares of the leachate internal errors. Importantly, the combined acetic acid wash (Table 3 and Fig. 2) plots within error of the isochron, indicating that any remnant surface contaminants were not a significant source of error. Terrestrial contamination of the lanthanides is not an issue for LAR 06319 (e.g., no Ce anomaly) as has been demonstrated with Pb isotopes in other martian meteorite samples (Gaffney et al., 2007).

The $\varepsilon Nd_I$ of $-7.21 \pm 0.41$ is within error of that of Zagami ($-7.0 \pm 0.02$ (Debaille et al., 2008)), NWA 1068 ($-7.0 \pm 0.2$ (Shih et al., 2003)), Shergotty ($-6.92 \pm 1.6$ (Bouvier et al., 2008)), and RBT 04262 ($-6.70 \pm 0.2$ (Shih et al., 2009)). The $\varepsilon Nd_I$ for LAR 06319 is slightly more enriched than Los Angeles ($-6.30 \pm 0.5$ (Bouvier et al., 2008) and NWA 856 ($-6.78 \pm 0.03$ (Brandon et al., 2004; Debaille et al., 2008)).

#### 4.2.2. Effects of leaching

The $^{147}Sm/^{144}Nd$ and $^{143}Nd/^{144}Nd$ ratios of the unleached bulk rock fraction (BR U) and the leachates of separate leached bulk rock fractions (BR 01N L, and BR 2N L-1st, Table 3) are nearly identical, indicating that the leached phase largely controls the REE budget in LAR 06319. Because the measured in-situ REE concentrations of phosphate phases are elevated by 1000–10,000 times relative to the other primary phases and form chondrite normalized REE patterns that are parallel to the bulk rock (Fig. 1), it is likely that phosphate largely controls the REE budget of LAR 06319 (~97% of the Nd and Sm; Tables 2 and 3). The isotopic composition of unleached hybrid-maskelynite (HMASK U) is also largely controlled by phosphate, as indicated by the unradiogenic $^{143}Nd/^{144}Nd$ ratio and elevated Sm and Nd concentrations relative to leached maskelynite (Table 3).

The bulk rock (as represented by the fines during crushing, Table 1) fractions BR 2N R-3rd and BR 2N R-4th were both processed in the same manner with identical leaching and chemical separation procedures. Despite the similarity in processing of these two bulk rock fractions, it appears that BR 2N R-3rd is dominated by maskelynite, as its $^{147}Sm$–$^{143}Nd$ isotope systematics are similar to the leached maskelynite fractions (Table 3 and Fig. 2). In contrast, BR 2N R-4th appears to be dominated by pyroxene based on $^{147}Sm$–$^{143}Nd$ isotope systematics that are similar to the leached pyroxene fractions (Table 3 and Fig. 2). The apparent mineralogic differences between these two bulk rock fractions likely resulted as a consequence of density induced grain settling during handling of the fines ($\geqslant$350 mesh grains) from which these two fractions were extracted. Maskelynite is less dense than pyroxene (~2.7 vs. ~3.4, respectively) and the BR 2N R-3rd could have preferentially sampled a maskelynite-rich sub-region of the fines. Subsequent extraction of fines for BR 2N R-4th then sampled more pyroxene-rich regions at the base of the vial. Hence, we believe density induced fractionation during handling is the best interpretation for the offset of BR 2N

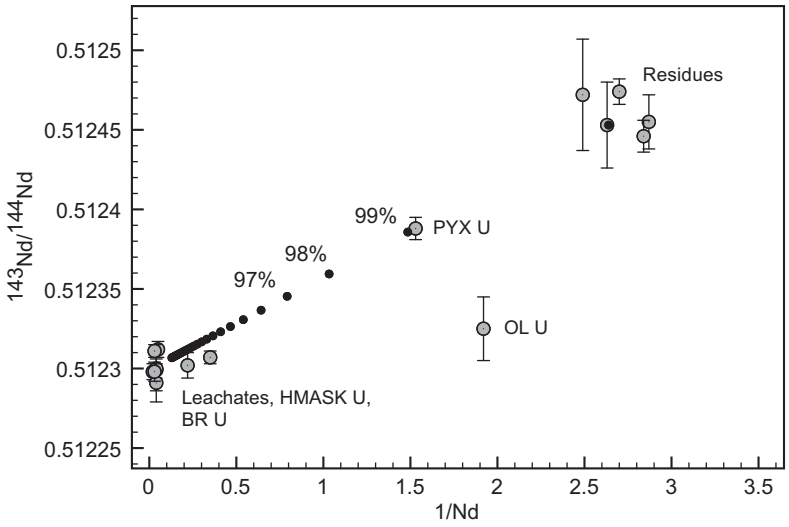


Fig. 3. Measured $^{143}Nd/^{144}Nd$ vs. 1/Nd. Linear arrays on this type of plot indicate mixing between two distinct reservoirs. In the case of the LAR 06319 isochron, one reservoir is similar to leached whole-rock (radiogenic $^{143}Nd/^{144}Nd$ and low Nd abundances) and the other is similar to the leachates (unradiogenic $^{143}Nd/^{144}Nd$ and high Nd abundances). The simplest explanation is that the isochron is essentially a mixing line between the bulk rock minus phosphate and phosphate. If the phosphate is not cogenetic with the rest of the rock, then this isochron has no age significance. OL U does not lie on this mixing line, but does fall on the isochron, suggesting that the phosphate controlled isochron is isochronous with the groundmass olivine and megacryst olivine. See text for further discussion.

R-3rd from the isochron (similar to that seen in fractions HMASK 2N R and HL-MASK 2N R) while BR 2N R-4th plots close to leached pyroxene residue and on the isochron.

The two maskelynite-rich fractions that plot off the isochron should be similar in terms of mineralogy, as the HMASK 2N R fraction (100–200 mesh) contains hybrid crystals composed primarily of maskelynite and HL-MASK 2N R (200–325 mesh) is a heavy liquid fraction that was designed to isolate pure maskelynite and grains composed primarily of maskelynite. Therefore, these two fractions are sampling similar grain populations with the primary difference being grain size. The offset from the isochron of the maskelynite-dominated fractions (BR 2N-3rd, HMASK 2N R, and HL-MASK 2N R) could result from decoupling of Sm from Nd that occurred during leaching. In theory, this should result in the residues offset to the left and their respective leachates being offset to the right of the isochron in order to balance the budgets of both elements and their isotopic compositions. However, all leachate samples, including those obtained from pyroxene-dominated and maskelynite-dominated fractions, have $^{147}Sm/^{144}Nd$ and $^{143}Nd/^{144}Nd$ ratios within uncertainty of each other (Table 3). The significantly greater Sm and Nd concentrations of the maskelynite leachates relative to their residues (approximately 30 ppm Nd, 13 ppm Sm vs. 0.35 ppm Nd, 0.175 ppm Sm, respectively) would leverage the offset so that the leachate $^{147}Sm/^{144}Nd$ ratio would not substantially change. For example, the amount of Sm that would need to be removed during leaching from HL-MASK 2N R if this sample originally plotted on the isochron is 11%, which would result in the $^{147}Sm/^{144}Nd$ composition of the leachate only changing 0.17%, a negligible effect. Although this scenario is unlikely because fractionation/decoupling of Sm from Nd during leaching is improbable (Mahlen et al., 2008), it cannot be completely discounted.

Residue–leachate pairs that form the radiogenic upper right and unradiogenic lower left portions of the isochron, respectively, largely determine the slope of the $^{147}Sm$–$^{143}Nd$ isochron (Fig. 2). The fraction PYX U plots nearly midway between the residue and leachate fields, while the remaining unleached samples plot close to the leachates. The relatively strong control that the leachate has on the isochron can be demonstrated by plotting the measured $^{143}Nd/^{144}Nd$ of the individual samples against their inverse Nd concentration (Fig. 3). With one exception, the LAR 06319 data form a rough linear array that can be modeled as two-component mixing (black dots in Fig. 3) between a reservoir with radiogenic and high $^{143}Nd/^{144}Nd$ and low Nd contents (leached bulk rock) and an unradiogenic and low $^{143}Nd/^{144}Nd$ and high Nd contents (phosphate). However, OL U does not plot on the linear array in Fig. 3, and hence, the $^{147}Sm$–$^{143}Nd$ isotopic composition of OL U is not controlled by phosphate and/or the radiogenic end-member that constrain the mixing array in Fig. 3. Because OL U plots on the $^{147}Sm$–$^{143}Nd$ isochron, this demonstrates that at least three phases (pyroxene, olivine, and phosphate) are recording a concordant age. Therefore, these data indicate that LAR 06319, on the scale of the bulk rock portion processed in this study, has remained effectively closed to Sm and Nd since formation of all phases with the exception of maskelynite.

#### 4.2.3. Origin of non-isochronous maskelynite

If Sm/Nd fractionation during leaching is not responsible for the isotopic composition of the maskelynite-rich points, then some other process must be invoked. The isotopic and chemical composition of the maskelynite-rich

points that lie above the isochron indicates that at least three components were involved in the maskelynitization process. Plagioclase and phosphate were involved as indicated from the trace element compositions and high-P contents of some of the maskelynite. However, plagioclase and phosphate have $^{147}Sm/^{144}Nd$ and $^{143}Nd/^{144}Nd$ ratios that are too low when combined to give the isotope systematics of the maskelynite-rich points. Hence, a third component must be present that has high $^{147}Sm/^{144}Nd$ and $^{143}Nd/^{144}Nd$. One possible phase is late-stage REE-enriched clinopyroxene (Borg et al., 2002). Plagioclase is a late crystallizing phase in LAR 06319 and is associated with evolved late-stage clinopyroxene compositions (Peslier et al., 2010). Clinopyroxene and maskelynite show evidence

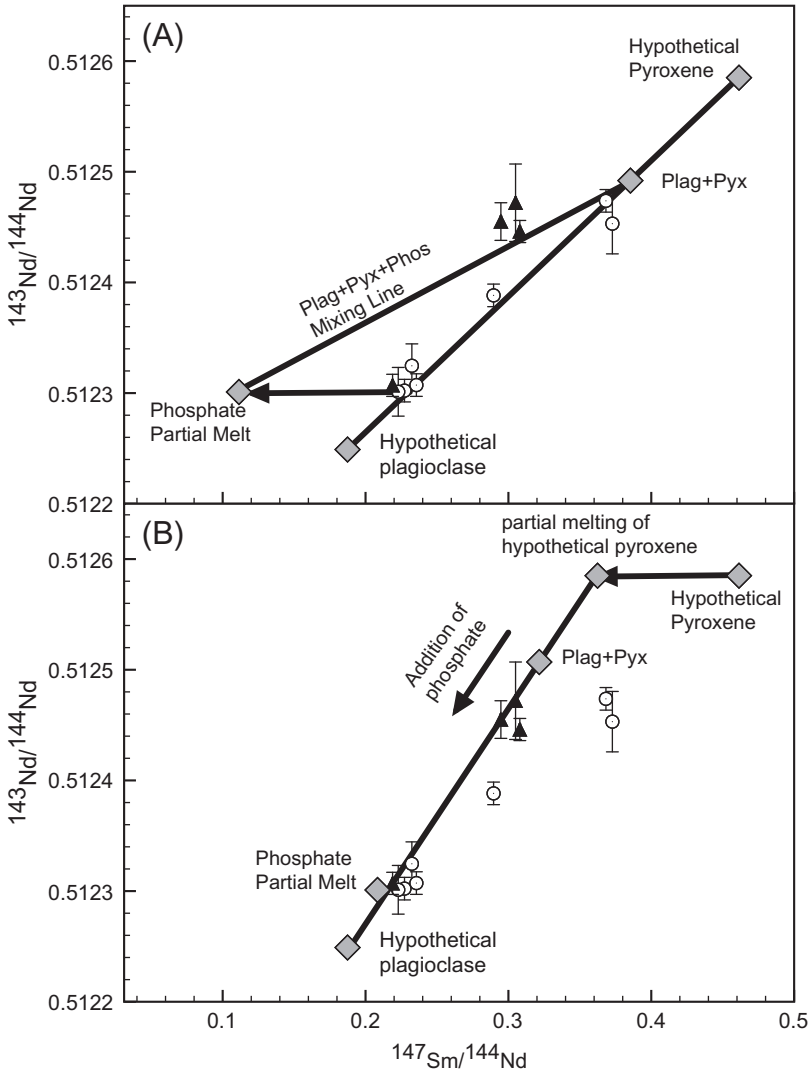


Fig. 4. The effect of mixing between plagioclase melt, pyroxene, and phosphate. (A) Mixing of plagioclase, pyroxene, and partial melt of phosphate. Composition of phases used for model: hypothetical plagioclase Sm = 0.031 ppm, Nd = 0.1 ppm, $^{147}Sm/^{144}Nd = 0.1874$, $^{143}Nd/^{144}Nd = 0.512249$; hypothetical pyroxene Sm = 0.464 ppm, Nd = 0.608 ppm, $^{147}Sm/^{144}Nd = 0.4614$, $^{143}Nd/^{144}Nd = 0.512585$; hypothetical phosphate melt Sm = 7 ppm, Nd = 38 ppm, $^{147}Sm/^{144}Nd = 0.1114$, $^{143}Nd/^{144}Nd = 0.512301$. Since pure plagioclase cannot be directly measured in LAR 06319 (all plagioclase has been converted to maskelynite, likely with minor assimilation of surrounding phases), the plagioclase composition has been estimated based on known partitioning behavior and the observation that plagioclase should have $^{147}Sm/^{144}Nd$ ratios less than the bulk rock as seen in other Martian meteorites (Borg et al., 2002; Shih et al., 2009). The hypothetical pyroxene composition is based on LA-ICP-MS analysis of a pigeonite rim composition with the highest Sm/Nd ratio. Hypothetical plagioclase and pyroxene are assumed to lie on the isochron, so $^{143}Nd/^{144}Nd$ ratios were calculated from the $^{147}Sm/^{144}Nd$ ratios. The plagioclase–pyroxene mixture is 30% pyroxene, 70% plagioclase. The isotopic composition of the three non-isochronous points can be modeled by addition of ~0.3% phosphate melt to the plagioclase–pyroxene mix. However, this model requires that Sm/Nd fractionation of phosphate during partial melting be much greater than suggested by phosphate *D* values. (B) Mixing of plagioclase, partial melt of pyroxene, and partial melt of phosphate. Plagioclase and pyroxene starting compositions are the same as in (A). Pyroxene liquids resulting from partial melting will lie on a horizontal line away from hypothetical pyroxene to the left of the isochron. The pyroxene partial melt point is the result of 11% partial melting. Mixing of pyroxene partial melt and plagioclase (~10% and 90%, respectively) with minor (~0.3%) phosphate melt can reproduce the isotopic composition of the non-isochronous points.

of melting to form discreet melt pockets, indicating that shock pressures and temperatures were high enough to locally melt pyroxene (Peslier et al., 2010). These observations show that clinopyroxene may also be involved in producing the maskelynite.

Based on this three-component mixture to account for the observed offset of points HMASK 2N R, HL-MASK 2N R, and BR 2N R-3rd, mixing between plagioclase, clinopyroxene, and phosphate melts is modeled here with the parameters listed in Fig. 4 and Table 4. Chen and El Goresy (2000) suggest that maskelynite is the result of complete melting of plagioclase, therefore, in all subsequent modeling it is assumed that plagioclase undergoes complete melting.

Two potential models are tested (Fig. 4). In one model, plagioclase and clinopyroxene are mixed in bulk (i.e., 100% melted) with a partial melt of phosphate (Fig. 4A). Plagioclase in martian meteorites has low Sm and Nd concentrations and $^{147}Sm/^{144}Nd$ ratios, and has a $^{143}Nd/^{144}Nd$ isotopic composition less radiogenic than the whole-rock (Borg et al., 2002; Shih et al., 2009). Clinopyroxene will have $^{147}Sm/^{144}Nd$ and $^{143}Nd/^{144}Nd$ ratios higher than the hybrid-pyroxene residues separated in this study. This is because any non-pyroxene components that were not removed by leaching (i.e., maskelynite and olivine) will have $^{147}Sm/^{144}Nd$ and $^{143}Nd/^{144}Nd$ ratios lower than clinopyroxene and force the isotopic composition down the isochron. Partial melts of phosphate will have a slightly lower $^{147}Sm/^{144}Nd$ ratio than present in the leachate samples. Using the partition coefficients for phosphate in Table 4, partial melting even as low as 0.01% will only lower the $^{147}Sm/^{144}Nd$ ratio by approximately 5%, instead of the required 50% needed to draw the maskelynite fractions from the isochron to their present position when mixed with phosphate and pyroxene (Fig. 4A). However, partition coefficients in phosphate can be highly variable due to surface-controlled partitioning (Rakovan et al., 1997) and disequilibrium conditions following the rapid increase in pressure and temperature following the shock event may have caused further fractionation. Hence, it is unclear whether the D values applied here for phosphate are realistic. Using these parameters, where it is assumed that phosphate partial melts result in a necessary 50% reduction in $^{147}Sm/^{144}Nd$, the approximate isotopic composition of the non-isochronous maskelynite-rich points can be modeled by a three-component mixture of these components, in proportions of approximately 70% plagioclase, 30% pyroxene, and 0.3% phosphate partial melt (Fig. 4A).

Although the above model could conceivably result in the position of the three points offset to the left of the isochron, an alternative model is the addition of a clinopyroxene partial melt to the plagioclase melt. A clinopyroxene partial melt will have a lower $^{147}Sm/^{144}Nd$ ratio than its residue (Table 4). This model can reproduce the isotopic composition of the three non-isochronous maskelynite-rich points by a mixture of approximately 90% plagioclase, 10% clinopyroxene melt, and 0.3% phosphate melt (Fig. 4B). This model may be more realistic because only

Table 4
Kd's between mineral and martian melts and parameters for REE crystallization model.

| | Clinopyroxene | Olivine | Oxide | Orthopyroxene | Plagioclase | Apatite | |
|---|---|---|---|---|---|---|---|
| La | 0.054 | 0.0004 | 0.00001 | 0.002 | 0.065 | 8.6 | |
| Ce | 0.0646 | 0.0005 | 0.00001 | 0.003 | 0.049 | 11.2 | |
| Nd | 0.107 | 0.001 | 0.00001 | 0.0068 | 0.104 | 14 | |
| Sm | 0.17 | 0.0013 | 0.00001 | 0.01 | 0.065 | 14.6 | |
| Eu | 0.28 | 0.0016 | 0.001 | 0.013 | 0.86 | 9.6 | |
| Gd | 0.32 | 0.0015 | 0.001 | 0.016 | 0.153 | 15.8 | |
| Tb | 0.31 | 0.0015 | 0.001 | 0.019 | 0.102 | 15.4 | |
| Dy | 0.33 | 0.0017 | 0.001 | 0.022 | 0.128 | *14.35* | |
| Er | 0.3 | 0.0015 | 0.001 | 0.03 | 0.137 | *11.6* | |
| Tm | 0.29 | 0.0015 | 0.01 | 0.04 | 0.122 | *9.8* | |
| Yb | 0.29 | 0.0015 | 0.01 | 0.049 | 0.141 | 8.1 | |
| Lu | 0.28 | 0.0015 | 0.01 | 0.06 | 0.19 | 8.1 | |
| Hf | 0.233 | 0.01 | 0.44 | 0.01 | 0.026 | 0.73* | |
| Zr | 0.233 | 0.01 | 0.44 | 0.01 | 0.026 | 0.73* | |
| | | | | | | | *F* |
| Stage 1 | 0 | 0 | 1 | 0 | 0 | 0 | 1 |
| Stage 2 | 0 | 0.95 | 0.05 | 0 | 0 | 0 | 0.98 |
| Stage 3 | 0.5 | 0.39 | 0.01 | 0.6 | 0 | 0 | 0.92 |
| Stage 4 | 0.798 | 0.2 | 0.002 | 0 | 0 | 0 | 0.78 |
| Stage 5 | 0.998 | 0 | 0.002 | 0 | 0 | 0 | 0.62 |
| Stage 6 | 0.998 | 0 | 0.001 | 0 | 0 | 0.001 | 0.46 |
| Stage 7 | 0.499 | 0 | 0.001 | 0 | 0.499 | 0.001 | 0.39 |

Data in italics is calculated by interpolation.
Clinopyroxene, olivine, oxide, and orthopyroxene partition coefficients from Borg and Draper (2003).
Plagioclase partition coefficients from Aignertorres et al. (2007).
Apatite partition coefficients from Paster et al. (1974). *Fujimaki (1986).
$F$ = fraction of liquid remaining at the beginning of each stage.
Mass fractions of crystallization phases for each stage from MELTS modeling of Peslier et al. (2010).

localized melting of pyroxene rims is observed (Peslier et al., 2010).

Mass balance mixing relationships indicate that ~6% phosphate is necessary to reproduce the $P_2O_5$ and REE composition of the high-P maskelynite. This is substantially greater than the ~0.3% indicated by the models. However, phosphate assimilation was not evenly distributed among all maskelynite since low-P maskelynite is also observed. Therefore, these mixing models based on $^{147}Sm$–$^{143}Nd$ isotope systematics suggest that the bulk amount of phosphate mixed into all maskelynite is much less than required by major and trace element mass balance calculations for only the high-P maskelynite.

The above models are non-unique and the specific mixing proportions are dependent upon the choice of starting compositions for the three phases involved and degrees of partial melting. However, these results demonstrate that although shock has had an effect on the $^{147}Sm$–$^{143}Nd$ systematics of LAR 06319, only the isotopic composition of maskelynite has been substantially affected.

#### 4.2.4. $^{176}Lu$–$^{176}Hf$ age and systematics

The $^{176}Lu$–$^{176}Hf$ age of LAR 06319 is 197 ± 29 Ma based on a five-point internal isochron (Table 3 and Fig. 5), with a derived initial $^{176}Hf/^{177}Hf$ isotope ratio of 0.282141 ± 0.000010 ($\varepsilon Hf_I = -18.0 \pm 0.4$ relative to CHUR). This age is concordant with the $^{147}Sm$–$^{143}Nd$ age of 183 ± 12 Ma presented here and with the $^{147}Sm$–$^{143}Nd$ and $^{87}Rb$–$^{87}Sr$ ages (190 ± 26 and 207 ± 14 Ma, respectively) of Shih et al. (2009). All fractions plot within error of the derived isochron and form a statistically significant line (Isoplot V3.7 derived Model 1 York fit, MSWD = 1.18). The $\varepsilon Hf_I$ of LAR 06319 is within error of those of Shergotty, Zagami, RBT 04262, and NWA 4468 (Blichert-Toft et al., 1999; Bouvier et al., 2005, 2008; Lapen et al., 2009). The separation of BR U from BR 01N R-1st and BR 2N R-1st is the result of the leaching procedure. Fraction BR U was washed in cold acetic acid while BR 01N R-1st and BR 2N R-1st were more aggressively leached in HCl. Previous work has shown that Lu and Hf are sensitive to the leaching procedure in fine-grained martian meteorite samples and that they can be decoupled even during a gentle leach (Lapen et al., 2008). In this sample, the leaching procedure did not result in decoupling of Lu from Hf, but instead resulted in correlated changes in $^{176}Lu/^{177}Hf$ ratio with the $^{176}Hf/^{177}Hf$ ratio such that the leaching procedure removed a radiogenic Hf phase that was in equilibrium with the bulk rock. Assuming that the radiogenic Hf phase(s) was homogeneously distributed throughout the bulk rock powder used for samples BR U, BR 01N, and BR 2N, ~67% of the Lu was removed during leaching as compared to <7% of the Hf. The resulting Lu/Hf ratio of the leached phase(s) (~1.23, $^{176}Lu/^{177}Hf = 0.175$) is consistent with phosphate as the leached phase. This is because the phosphate has Lu/Hf = 0.91, whereas olivine, pyroxene, and maskelynite have Lu/Hf ≪ 1 (Table 2). There is no correlation between measured $^{176}Hf/^{177}Hf$ and 1/Hf, indicating that the isochron is not an artifact of mixing (Fig. 6) The maskelynite process that affected the Sm–Nd systematics is unlikely to greatly affect the Lu–Hf systematics because plagioclase tends to have a Lu/Hf ratio greater than the bulk rock.

### 4.3. Crystallization ages of shergottites

Four internal isochron ages using three separate chronometers have been determined on LAR 06319. The ages range from 183 ± 12 Ma ($^{147}Sm$–$^{143}Nd$ presented here) to 207 ± 14 Ma (Shih et al., 2009). However, the four ages are within uncertainty of each other and are therefore concordant (Fig. 7). The weighted average (calculated using Isoplot V3.7) of the four concordant radiometric ages obtained for LAR 06319 is 193 ± 20 Ma ($2\sigma$). This age agrees well with the ~150–230 Ma internal isochron ages of other

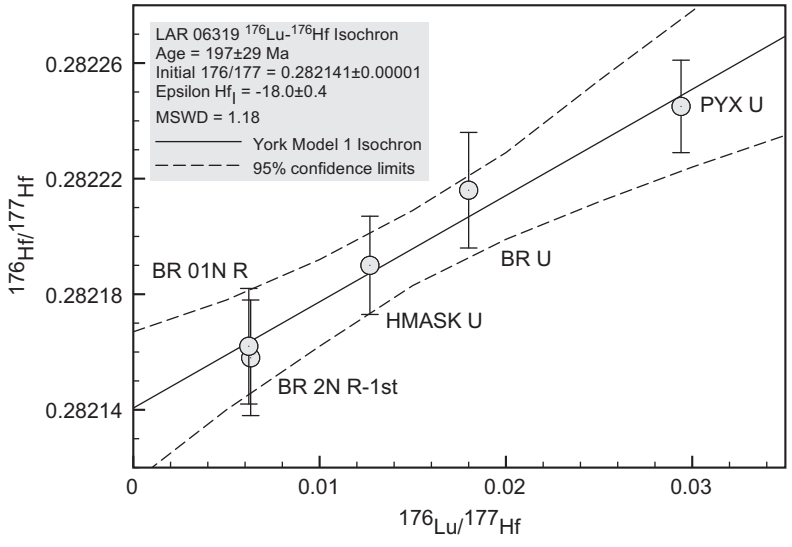


Fig. 5. Internal mineral $^{176}Lu$–$^{176}Hf$ isochron for LAR 06319. The $^{176}Lu$–$^{176}Hf$ age is 197 ± 29 Ma with an initial $^{176}Lu/^{177}Hf$ ratio of 0.282141 ± 10 (−18.0 ± 0.4 $\varepsilon Hf_I$ relative to CHUR; present day $^{176}Hf/^{177}Hf = 0.282772$, $^{176}Lu/^{177}Hf = 0.0332$, $^{176}Lu$ decay constant = $1.87 \times 10^{11}$ yr$^{-1}$ (Blichert-Toft and Albarede, 1997)). The program Isoplot V3.7 was used to generate a Model 1 isochron with a MSWD of 1.18.

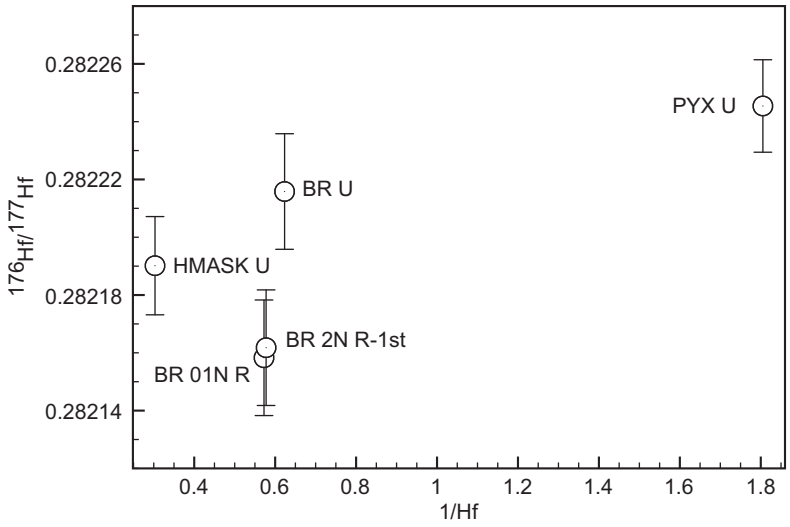


Fig. 6. Measured $^{176}Hf/^{177}Hf$ vs. 1/Hf. There is no correlation between measured isotopic ratio and inverse concentration, indicating that the phosphate control seen in the $^{147}Sm$–$^{143}Nd$ isochron is non-existent in the $^{176}Lu$–$^{176}Hf$ isochron.

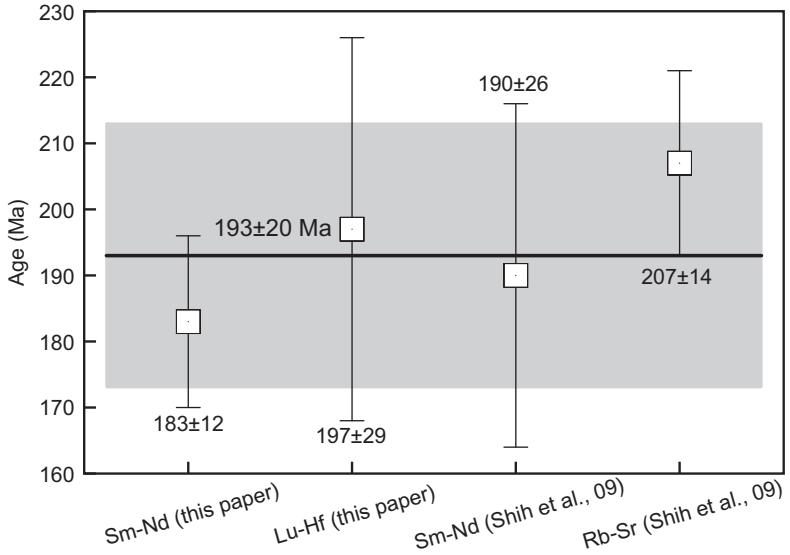


Fig. 7. Summary of radiometric ages for LAR 06319. The weighted average (calculated using Isoplot V3.7) of the four ages is 193 ± 20 Ma ($2\sigma$).

enriched shergottites (Borg et al., 2002; Shih et al., 2003, 2009; Bouvier et al., 2005, 2008; Lapen et al., 2009).

The geologic significance of the internal isochrons in shergottites has been recently discussed. Bouvier et al. (2005, 2008, 2009) interpret $^{207}Pb$–$^{206}Pb$ ages of leached bulk rock and mineral separate fractions of Shergotty, Zagami, and Los Angeles to indicate 4.1–4.3 Ga igneous crystallization ages. These authors interpret the younger $^{147}Sm$–$^{143}Nd$, $^{87}Rb$–$^{87}Sr$, and $^{176}Lu$–$^{176}Hf$ internal isochrons for shergottites to reflect resetting by much later events. In contrast, Gaffney et al. (2007) interpret their $^{207}Pb$–$^{206}Pb$ isochron age of 4.3 Ga for QUE 94201 as indicative of incomplete removal of modern terrestrial Pb during leaching and thus assign no age significance to the $^{207}Pb$–$^{206}Pb$ isotope data. The Pb isotope systematics of QUE 94201 indicate that there are three sources of Pb, (1) initial Pb present during crystallization, (2) radiogenic Pb, and (3) modern terrestrial Pb (Gaffney et al., 2007). It is this third source of Pb that dominates the leachate fractions and predominantly defines the apparently old $^{207}Pb$–$^{206}Pb$ isochron ages for QUE 94201. Since shergottites are characterized by a relatively low U/Pb ratio (Borg et al., 2005), the ingrowth of radiogenic Pb over time since crystallization is relatively minor. In that case, the three-component mixing scenario suggested by Gaffney et al. (2007) essentially devolves into a binary mixing between unradiogenic martian primordial Pb and radiogenic terrestrial Pb instead of a cloud of points as suggested by Bouvier et al. (2008). In addition, Zagami leachates form an array with a slope corresponding to an age of ~4 Ga on a

$^{207}Pb$–$^{206}Pb$ plot. Common terrestrial Pb also lies along this line, suggesting that the leachate samples are mixtures of common terrestrial Pb and primordial Zagami Pb. However, Borg et al. (2005) found that leached residues of their purest mineral fractions yielded an $^{238}U/^{206}Pb$ age of 156 ± 6 Ma that is concordant with $^{147}Sm$–$^{143}Nd$, $^{87}Rb$–$^{87}Sr$, and $^{176}Lu$–$^{176}Hf$ internal isochrons. These same fractions form a line subparallel to a 166 Ma reference line on a $^{207}Pb$–$^{206}Pb$ plot. Thus the $^{238}U$–$^{206}Pb$ and $^{207}Pb$–$^{206}Pb$ isotopic systematics in Zagami indicate that, although disturbed, evidence of young ages can be gleaned from these systems. Jagoutz (1991), on the other hand, originally interpreted the 4.1–4.3 Ga $^{207}Pb$–$^{206}Pb$ isotope systematics for shergottites as reflecting their mantle source closure times, but did not assign chronometric significance to the $^{207}Pb$–$^{206}Pb$ data in terms of their crystallization ages.

The concordant ages of three isotopic systems ($^{147}Sm$–$^{143}Nd$, $^{87}Rb$–$^{87}Sr$, and $^{176}Lu$–$^{176}Hf$) that give an average age of 193 ± 20 Ma for LAR 06318 provides the opportunity to evaluate whether these concordant ages reflect the crystallization age of this stone, or if the measured ages of LAR 06319 and the other shergottites instead reflect shock resetting or shock-induced metamorphism and/or metasomatism. In the latter case, the younger ages must reflect a mechanism that results in pervasive resetting of the $^{147}Sm$–$^{143}Nd$, $^{87}Rb$–$^{87}Sr$, and $^{176}Lu$–$^{176}Hf$ systems while preserving only the $^{207}Pb$–$^{206}Pb$ isotopic signatures for the original age of magmatic crystallization.

Possible mechanisms that could reset these chronometers to younger ages are fluid induced alteration and/or metasomatism or impact induced pressurized filtration (Bouvier et al., 2005, 2008). In particular, percolation of mildly acidic fluids during final drying of lakes or seas late in martian history could have reset the chronometers hosted in the phosphate phases. As noted by Basu Sarbadhikari et al. (2009) and in the discussion above, phosphate is the primary REE carrier in LAR 06319 and other shergottites. If the $^{147}Sm$–$^{143}Nd$, $^{87}Rb$–$^{87}Sr$, and $^{176}Lu$–$^{176}Hf$ internal isochron ages for LAR 06319 reflect a late fluid mobilization event, the phosphate dominated leachates, bulk rock residues, and purified mineral separates must have undergone complete resetting through a mechanism of parent–daughter isotope exchange. If this is the case, there should be evidence of fluid infiltration such as hydrous minerals, although the lack of such minerals cannot be considered strictly diagnostic of no fluid interaction. Hydrous minerals are completely absent in LAR 06319 with one exception. This exception is a single amphibole crystal found in a melt inclusion (Basu Sarbadhikari et al., 2009), which is likely the result of incomplete degassing of volatiles trapped in the inclusion during magmatic crystallization rather than evidence of bulk rock interaction with fluids. Mineralogical features indicative of fluid–rock interaction are not present, indicating that if fluid infiltration is responsible for any potential isotopic resetting, it did so as a cryptic process along grain boundaries (Zindler and Jagoutz, 1988) without disturbing the interior mineral REE concentrations and zonation patterns. If such a cryptic process did occur, it does not explain why leached pure mineral separates, which have had cryptic material on their grain boundaries removed during leaching are isochronous with bulk rock samples and leachates. The adherence of these phases for the three isotopic systems to concordant isochrons is strong evidence that grain boundary disturbances played no part in creating the age relationships observed. Alteration or metasomatism of phosphates by fluids was also invoked to explain bulk rock $^{147}Sm/^{144}Nd$ ratios in shergottites that are greater than expected from their corresponding $^{143}Nd/^{144}Nd_I$ (Blichert-Toft et al., 1999). However, this feature can be explained through melt extraction just prior to the melting that produced the shergottites from their source region, which results in a change in the Sm/Nd ratio without corresponding evolution of the $^{143}Nd/^{144}Nd$ ratio (Borg et al., 1997; Debaille et al., 2008). Therefore, it appears that fluid alteration or metasomatism has not influenced the $^{147}Sm$–$^{143}Nd$ and $^{176}Lu$–$^{176}Hf$ isotopic systematics of LAR 06319.

Another possible mechanism for resetting the lithophile chronometers to younger ages is shock or heating experienced prior to or during ejection from Mars' surface (Jagoutz, 1989; Nyquist et al., 1991a,b; Borg et al., 1999). Evidence for shock in LAR 06319 is abundant. Plagioclase in LAR 06319 is completely converted to maskelynite. Highly fractured olivine megacrysts and pyroxenes are common as are shock melt patches. A large shock melt vein cuts through one thick section of LAR 06319 (Basu Sarbadhikari et al., 2009). Hence, while LAR 06319 is undoubtedly shocked, it is unlikely to have caused isotopic resetting with the exception of maskelynite for $^{147}Sm$–$^{143}Nd$ as noted above. In the case of shock or thermal redistribution of trace elements, the present day bulk rock $^{143}Nd/^{144}Nd$ or $^{176}Hf/^{177}Hf$ ratios would represent the time-integrated bulk rock composition since crystallization as long as the rock has remained a closed system with regard to trace elements. In such a case, individual mineral fractions may become altered (i.e., maskelynite) and Sm, Nd, Lu, and Hf may be redistributed throughout the rock, but the bulk rock isotopic composition does not change as a result of the shock. Fraction BR U represents the best estimate for the bulk rock isotopic composition of this stone if LAR 06319 has remained closed to Sm, Nd, Lu, and Hf since crystallization. Supporting evidence for this assumption is that BR U plots with the other enriched shergottites on a plot of the time-integrated mantle source $^{147}Sm/^{144}Nd$ ratio vs. the measured $^{147}Sm/^{144}Nd$ ratio (Fig. 8). The mantle source $^{147}Sm/^{144}Nd$ ratio is calculated by using the isochron initial $^{143}Nd/^{144}Nd$ ratio of each shergottite and the following assumptions. First, differentiation from bulk Mars (assumed to be chondritic) occurred in two stages. Second, the source differentiated at 4.5685 Ga and evolved with constant parent/daughter ratios until the sample was extracted from the mantle at their crystallization age (Debaille et al., 2007). Initial $^{143}Nd/^{144}Nd$ ratios of LAR 06319 fractions were calculated using the internal $^{147}Sm$–$^{143}Nd$ isochron age. The shergottite array on this diagram is interpreted to be a mixing line between early-formed enriched and depleted mantle domains (Debaille et al., 2007; Lapen et al., 2010). Because BR U plots with the rest of the enriched shergottites in this diagram, this shows that BR U is a good representation of the bulk rock composition. Fig. 8 also

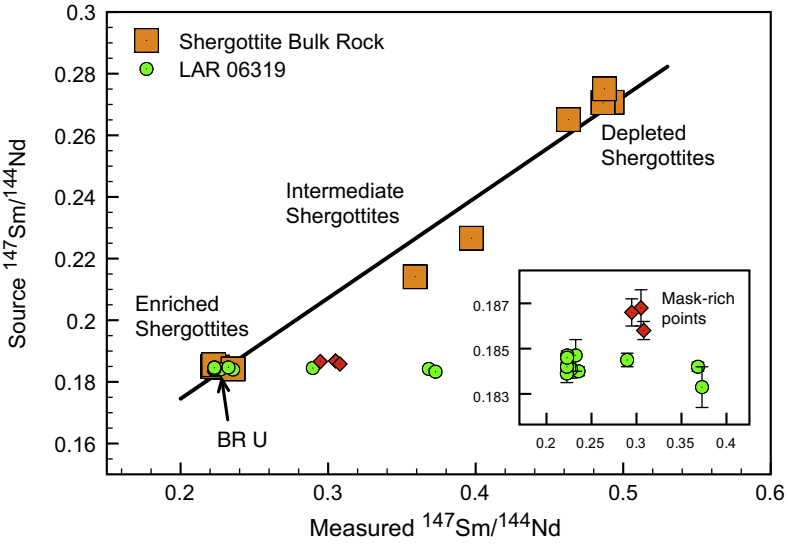


Fig. 8. Measured $^{147}Sm/^{144}Nd$ vs. Source $^{147}Sm/^{144}Nd$ for LAR 06319 fractions and shergottite bulk rocks. Source $^{147}Sm/^{144}Nd$ is calculated assuming two-stage differentiation from a chondritic bulk Mars (Debaille et al., 2007), 1st stage differentiation from bulk Mars (i.e., CHUR) at 4.5685 Ga, and source formation age equal to the isochron age of each shergottite. $\lambda_{Sm} = 6.54 \times 10^{-12}$, $^{143}Nd/^{144}Nd_{CHUR} = 0.512638$, $^{147}Sm/^{144}Nd_{CHUR} = 0.1967$. The trend formed by the enriched, intermediate, and depleted shergottites has been interpreted as a mixing line representing mixing of early-formed enriched and depleted mantle domains formed during magma ocean differentiation (Debaille et al., 2007; Lapen et al., 2010). The LAR 06319 BR U fraction plots directly with the enriched shergottites, suggesting that this fraction is adequately representative of the true bulk rock composition of LAR 06319. Significantly, the rest of the fractions plot within error of a horizontal line, with the exception of the three points that do not plot on the isochron (shown on this plot in red), indicating that all fractions had the same $^{147}Sm/^{144}Nd$ at the time of crystallization. This is further evidence that these phases are cognate and have not been disturbed. (For interpretation of the references to color in this figure legend, the reader is referred to the web version of this article.)

provides further evidence that the $^{147}Sm$–$^{143}Nd$ isochron presented here is unaltered (with the exception of the maskelynite-dominated fractions that lie above the isochron, as previously discussed) because the calculated source $^{147}Sm/^{144}Nd$ ratios for each data point that plot along the isochron form a horizontal line (within error) indicating that each fraction had the same source $^{147}Sm/^{144}Nd$ at crystallization, which is equivalent to all phases having the same initial $^{143}Nd/^{144}Nd$ ratio. Later alteration of individual fractions would cause the source $^{147}Sm/^{144}Nd$ to deviate from a horizontal line as is seen in the maskelynite-rich fractions.

Assuming that BR U is representative of the time-integrated bulk rock composition since crystallization, if LAR 06319 crystallized at 4.1 Ga the $^{176}Lu/^{177}Hf$ ratio of its mantle source (assuming differentiation from CHUR at 4.5685 Ga) would be 0.0942, a value that is difficult to envision geologically, as values this high suggest an extraordinarily depleted source (e.g., Earth's depleted mantle has a model $^{176}Lu/^{177}Hf$ ratio of 0.045 (Salters and Stracke, 2004)). This is also opposite to the incompatible trace element enriched character of its source obtained via all other geochemical parameters. The same procedure for Sm/Nd results in a negative source $^{147}Sm/^{144}Nd$ ratio of −0.25, which is not possible. In summary, while a shock event may have caused internal decoupling of Sm from Nd via reaction between plagioclase melt, pyroxene, and phosphate on a small scale, these observations indicate that LAR 06319 was closed at the bulk rock scale. Hence, the internal isochrons from three separate systems cannot be interpreted as resulting from shock resetting.

### 4.4. Trace element modeling

Previous detailed petrographic studies (Basu Sarbadhikari et al., 2009; Peslier et al., 2010) have concluded that LAR 06319 is the result of fractional crystallization of a single batch of magma in a closed system. If this is the case, then trace element zonation profiles of pyroxene phenocrysts should be consistent changes in magma composition caused by fractional crystallization (Wadhwa et al., 1994). In order to model the trace element evolution of LAR 06319, it is necessary to estimate the trace element content of the parent magma and know the percentage of crystallizing phases throughout the crystallization sequence. Because of their strongly incompatible nature the REE were modeled along with the HFSE's (high field strength element) Zr and Hf. The parent magma REE, Zr, and Hf abundances were estimated by calculating the REE, Zr, and Hf concentrations of the liquid in equilibrium with the most magnesian pyroxene using the crystal/liquid partition coefficients ($D$) of Borg and Draper (2003) for martian compositions. The selection of appropriate $D$ values is difficult because there are few studies aimed at determining appropriate $D$ values for shergottite magmas. Studies on clinopyroxene partitioning in synthetic shergottitic magmas indicate that although there are broad similarities to terrestrial systems, direct use of terrestrial $D$ values may not be entirely appropriate (McKay et al., 1986). Therefore, we employ the $D$ values of Borg and Draper (2003) that were used to model crystallization of a martian magma ocean. The majority of the values in their compilation are from

Snyder et al. (1992), which used these *D* values to model the crystallization of the lunar magma ocean. The *D* values for clinopyroxene in Snyder et al. (1992) are from the McKay et al. (1986) synthetic shergottite partitioning study. Because clinopyroxene, to a large degree, controls the trace element partitioning in mafic systems (since it has the highest *D* values for a range of incompatible trace elements), the fact that these *D* values are specifically for martian compositions is important for the models presented in this section. Although olivine was the first major phase on the liquidus, its REE, Zr, and Hf element abundances are generally at or below the detection limit of the LA-ICP-MS method. Because pyroxene is a stable phase nearly throughout the entire crystallization sequence and generally has measurable REE, Zr, and Hf contents, it is better suited to examine the REE, Zr, and Hf evolution during crystallization. The model parent magma REE, Zr, and Hf contents calculated from the most Mg-rich pyroxenes are approximately flat at 10× chondritic. They are subparallel to that of bulk rock and a melt inclusion from an olivine megacryst and are very similar to previous estimates of parental melt composition (see Fig. 12 of Basu Sarbadhikari et al., 2009). The close match between the modeled results from early-crystallized orthopyroxene and the bulk rock and melt inclusion indicates that the orthopyroxene is recording equilibrium with the true parent melt. Because of this close agreement, for all subsequent modeling, the parent magma REE, Zr, and Hf concentrations are assumed to be identical to that of the melt inclusion (Table 2).

Results from the crystallization sequence modeling by Peslier et al. (2010) using MELTS (Ghiorso and Sack, 1995), were used to estimate the phase proportions and compositions and fraction of liquid remaining at the arrival or departure of a phase from the liquidus. Equilibrium and fractional crystallization of the calculated parent magma was modeled using a seven-stage crystallization sequence (Table 4) that closely matches the observed petrography (Peslier et al., 2010).

Pyroxene compositions in equilibrium with the model liquids were compared to the measured pyroxene REE, Zr, and Hf abundances (Fig. 9). Orthopyroxene LA-ICP-MS results are nearly identical to those generated by both the fractional and equilibrium crystallization models. Clinopyroxene arrives on the liquidus at 78% liquid remaining and continues to crystallize throughout the rest of the sequence. The measured pigeonite composition is a very close match to early-crystallized model clinopyroxene. No measured clinopyroxene compositions match the composition of the late-stage model clinopyroxene, although this is likely because the late-stage clinopyroxene is present as thin Fe-rich rims around the more Mg-rich clinopyroxene cores (Peslier et al., 2010). The Fe-rich rims are too thin to be quantitatively sampled via laser ablation, making the measured clinopyroxene compositions biased towards the more Mg-rich near edge and interior compositions. The lower range of the measured clinopyroxene REE, Zr, and Hf contents is below the lowest model clinopyroxene REE concentrations, which potentially indicates that clinopyroxene crystallization commenced earlier in the crystallization sequence than assumed in the model or that the primitive melt composition is too enriched in REE.

A key interpretation from the isotope systematics is that phosphate is in isotopic equilibrium with the primary silicate phases. The fractional crystallization model provides one further test regarding the nature of the phosphate—if the phosphate concentrations can be reproduced by the

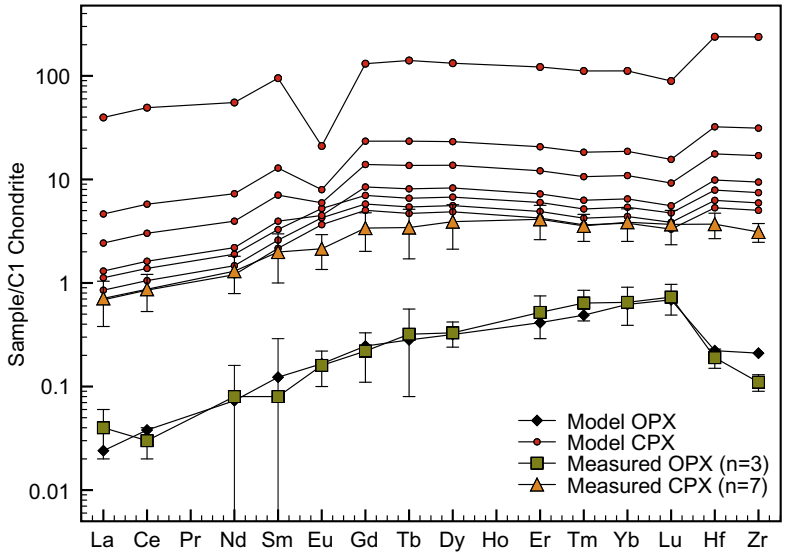


Fig. 9. Chondrite normalized REE, Zr, and Hf profiles of measured orthopyroxene (average, $n = 3$) and clinopyroxene (average, $n = 7$) compared to model pyroxene compositions from fractional crystallization (Peslier et al., 2010) of the estimated LAR 06319 parent magma. Error bars on the measured OPX and CPX compositions are the standard deviation of the averaged compositions. The fractional crystallization model closely reproduces the measured orthopyroxene compositions. Measured clinopyroxene REE abundances have slightly less pronounced LREE depletions than the model compositions, but overall, match the model closely. The range in model clinopyroxene compositions is from the start of clinopyroxene crystallization at Stage 4 of the crystallization model, clinopyroxene composition at Stage 5, Stage 6, and Stage 7, and then clinopyroxene composition at 30%, 20%, 10%, and 1% liquid remaining.

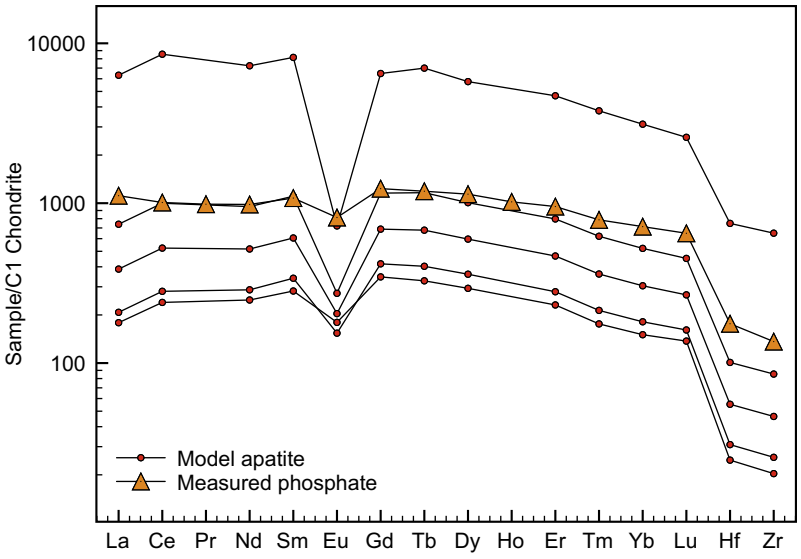


Fig. 10. Chondrite normalized REE, Zr, and Hf profiles of measured phosphate compared to model apatite compositions from fractional crystallization (Peslier et al., 2010) of the estimated LAR 06319 parent magma. The measured REE, Zr, and Hf abundances of the phosphate match the model composition fairly well, except for slightly more elevated HREE and a less pronounced Eu anomaly. The model phosphate compositions shown are the beginning of phosphate crystallization at Stage 6, phosphate at Stage 7, and then 30%, 20%, 10%, and 1% liquid remaining. Error bars for measured phosphate concentrations are smaller than the symbols.

fractional crystallization of the estimated LAR 06319 parental magma it is extremely likely that the trace element and isotopic compositions observed in LAR 06319 are the result of closed-system processes and that no open system mobilization of REE, Zr, and Hf has taken place. Following the same procedures to estimate the model pyroxene compositions, the model phosphate abundances range from approximately 200× chondrite at the beginning of phosphate crystallization to ~6000× chondrite (Fig. 10). The REE, Zr, and Hf profile is gently concave upwards, but approximately flat, with a pronounced downward Eu anomaly. These profiles are very similar to the ~1000× chondrite measured phosphate REE, Zr, and Hf profile. The Eu anomaly on the measured phosphate is not nearly as pronounced as in the model, but overall, the measured phosphate appears to be in equilibrium with liquid remaining after ~90% fractional crystallization. This is in accord with petrographic evidence that the phosphate is a late-stage product of crystallization (Basu Sarbadhikari et al., 2009; Peslier et al., 2010).

The isotopic systematics, LA-ICP-MS results, and trace element modeling are most consistent with progressive closed-system fractional crystallization of a single REE, Zr, and Hf enriched magma. While models that invoke enrichments in incompatible trace elements in shergottites by an assimilation and fractional crystallization scenario involving a depleted magma assimilating an enriched component (e.g., crust) have been advanced (Jones, 1986; Rumble and Irving, 2009), the REE, Zr, and Hf zonations in LAR 06319 pyroxene do not support those conclusions, nor does the Re–Os isotopic evidence (Brandon et al., 2000). The cores of early-formed orthopyroxene are in equilibrium with an incompatible trace element enriched parent liquid. Fractional crystallization of this liquid can then produce compositions similar to measured pigeonite and phosphate. The consistent trace element concentrations of the pyroxene phenocrysts and the observed isotopic equilibrium between the phosphate and olivine megacrysts suggest that these phases in LAR 06319 exhibit the original magmatic trace element characteristics. Hence, we reemphasize the point that the trace element and petrographic data from LAR 06319 strongly argues that there has been no pervasive metasomatism or aqueous alteration that could have caused chronometric resetting, nor has there been bulk rock scale open system remobilization of the trace elements from shock with the exception of Sm and/or Nd in plagioclase during maskelynitization. In summary, the trace element models presented here are consistent with the interpretation that the isotopic results are recording the true crystallization age of LAR 06319.

## 5. CONCLUSIONS AND IMPLICATIONS

The martian meteorite LAR 06319 has an internal $^{147}Sm$–$^{143}Nd$ isochron age of $183 \pm 12$ Ma and an internal $^{176}Lu$–$^{176}Hf$ isochron age of $197 \pm 29$ Ma. These two ages, taken together with previously determined internal isochron ages (Shih et al., 2009), yield a weighted average age of $193 \pm 20$ Ma. This age is the best estimate of the crystallization age of LAR 06319. The isotopic systematics of LAR 06319 may be best explained that plagioclase reacted with partial melts of pyroxene and phosphate during the maskelynitization process resulting in decoupling of Sm and Nd. However, at the bulk rock level, LAR 06319 remained a closed system and all other fractions (bulk rock, olivine, pyroxene, and phosphate) are in isotopic equilibrium. The incompatible trace element systematics are consistent with progressive crystallization of an incompatible

element enriched magma. These data rule out the possibility of assimilation of an enriched component into a depleted magma or late-stage metasomatism/alteration as the cause of the enriched incompatible element nature of LAR 06319. All lines of evidence indicate that the isotopic and trace element characteristics of LAR 06319 (with the exception of maskelynite) are the result of equilibrium igneous processes and that the internal mineral isochron ages are recording the true crystallization age of the rock. Our results on LAR 06319 reinforce the interpretation of the ~150–575 Ma crystallization ages for the other shergottites as magmatic ages, and suggest that the $^{207}Pb$–$^{206}Pb$ isotopic data do not reflect igneous crystallization in the Noachian. These conclusions are consistent with updated crater counting results based on new high-resolution imagery that suggest young surface regions are much more widespread than previously thought (Neukum et al., 2010). Consequently, the predominance of young martian meteorites may not be unexpected, especially when it is considered that the ejection of meteorites from the ancient, heavily fractured, and likely altered Noachian crustal units appears to be unlikely (Hartmann and Barlow, 2006).

## ACKNOWLEDGMENTS

J.S. was supported on a Lunar and Planetary Institute postdoctoral fellowship during the analytical phase of this work. A.D.B. and T.L.J. acknowledge support for their respective NASA Cosmochemistry awards. T.J.L. also acknowledges the University of Houston Institute for Space System Operations for partially supporting the analytical campaign at UW-Madison. NASA and the Antarctic Meteorite Working Group are thanked for providing the sample of LAR 06319 examined in this study. We thank reviewers James Day, Audrey Bouvier, and an anonymous reviewer for constructive and helpful reviews and editor Richard Walker for his efficient editorial handling of the manuscript.

## REFERENCES

Aignertorres M., Blundy J., Ulmer P. and Pettke T. (2007) Laser ablation ICPMS study of trace element partitioning between plagioclase and basaltic melts: an experimental approach. *Contrib. Mineral. Petrol.* **153**, 647–667.

Barrat J., Blichert-Toft J., Nesbitt R. and Keller F. (2001) Bulk chemistry of Saharan shergottite Dar al Gani 476. *Meteorit. Planet. Sci.* **36**, 23–29.

Barrat J., Jambon A., Bohn M., Gillet P., Sautter V., Göpel C., Lesourd M. and Keller F. (2002) Petrology and chemistry of the Picritic Shergottite North West Africa 1068. *Geochim. Cosmochim. Acta* **66**, 3505–3518.

Basu Sarbadhikari A., Day J., Liu Y., Rumble, III, D. and Taylor L. (2009) Petrogenesis of olivine-phyric shergottite Larkman Nunatak 06319: implications for enriched components in martian basalts. *Geochim. Cosmochim. Acta* **73**, 2190–2214.

Blichert-Toft J. and Albarede F. (1997) The Lu–Hf isotope geochemistry of chondrites and the evolution of the mantle–crust system. *Earth Planet. Sci. Lett.* **148**, 243–258.

Blichert-Toft J., Gleason J., Télouk P. and Albarede F. (1999) The Lu–Hf isotope geochemistry of shergottites and the evolution of the Martian mantle–crust system. *Earth Planet. Sci. Lett.* **173**, 25–39.

Borg L. and Draper D. (2003) A petrogenetic model for the origin and compositional variation of the martian basaltic meteorites. *Meteorit. Planet. Sci.* **38**, 1713–1731.

Borg L., Nyquist L., Taylor L., Wiesmann H. and Shih C.-Y. (1997) Constraints on Martian differentiation processes from Rb–Sr and Sm–Nd isotopic analyses of the basaltic shergottite QUE 94201. *Geochim. Cosmochim. Acta* **61**, 4915–4931.

Borg L., Norman M., Nyquist L., Bogard D., Taylor L. and Lindstrom M. (1999) Isotopic studies of ferroan anorthosite 62236: a young lunar crustal rock from a light rare-earth-element-depleted source. *Geochim. Cosmochim. Acta* **63**, 2679–2691.

Borg L., Nyquist L., Wiesmann H. and Reese Y. (2002) Constraints on the petrogenesis of Martian meteorites from the Rb–Sr and Sm–Nd isotope systematics of the lherzolite shergottites ALH77005 and LEW88516. *Geochim. Cosmochim. Acta* **66**, 2937–2953.

Borg L., Nyquist L., Wiesmann H., Shih C.-Y. and Reese Y. (2003) The age of Dar al Gani 476 and the differentiation history of the martian meteorites inferred from their radiogenic isotopic systematics. *Geochim. Cosmochim. Acta* **67**, 3519–3536.

Borg L., Edmunson J. and Asmerom Y. (2005) Constraints on the U–Pb isotopic systematics of Mars inferred from a combined U–Pb, Rb–Sr, and Sm–Nd isotopic study of the Martain meteorite Zagami. *Geochim. Cosmochim. Acta* **69**, 5819–5830.

Bouvier A., Blichert-Toft J., Vervoort J. and Albarede F. (2005) The age of SNC meteorites and the antiquity of the Martian surface. *Earth Planet. Sci. Lett.* **240**, 221–233.

Bouvier A., Blichert-Toft J., Vervoort J., Gillet P. and Albarede F. (2008) The case for old basaltic shergottites. *Earth Planet. Sci. Lett.* **266**, 105–124.

Bouvier A., Blichert-Toft J. and Albarede F. (2009) Martian meteorite chronology and the evolution of the interior of Mars. *Earth Planet. Sci. Lett.* **280**, 285–295.

Brandon A., Walker R., Morgan J. and Goles G. (2000) Re–Os isotopic evidence for early differentiation of the Martian mantle. *Geochim. Cosmochim. Acta* **64**, 4083–4095.

Brandon A., Nyquist L., Shih C.-Y. and Wiesmann H. (2004) Rb–Sr and Sm–Nd isotope systematics of shergottite NWA 856: crystallization age and implications for alteration of hot desert SNC meteorites. *Lunar Planet. Sci. XXXV*. Lunar Planet. Inst., Houston. #1931 (abstr.).

Chen M. and El Goresy A. (2000) The nature of maskelynite in shocked meteorites: not diaplectic glass but a glass quenched from shock-induced dense melt at high pressures. *Earth Planet. Sci. Lett.* **179**, 489–502.

Crozaz G. and Wadhwa M. (2001) The terrestrial alteration of Saharan Shergottites Dar al Gani 476 and 489: a case study of weathering in a hot desert environment. *Geochim. Cosmochim. Acta* **65**, 971–978.

Debaille V., Brandon A., Yin Q. and Jacobsen B. (2007) Coupled $^{142}Nd$–$^{143}Nd$ evidence for a protracted magma ocean in Mars. *Nature* **450**, 525–528.

Debaille V., Yin Q.-Z., Brandon A. and Jacobsen B. (2008) Martian mantle mineralogy investigated by the $^{176}Lu$–$^{176}Hf$ and $^{147}Sm$–$^{143}Nd$ systematics of shergottites. *Earth Planet. Sci. Lett.* **269**, 186–199.

Fujimaki H. (1986) Partition-coefficients of Hf, Zr, and Ree between zircon, apatite, and liquid. *Contrib. Mineral. Petrol.* **94**, 42–45.

Gaffney A., Borg L. and Connelly J. (2007) Uranium–lead isotope systematics of Mars inferred from the basaltic shergottite QUE 94201. *Geochim. Cosmochim. Acta* **71**, 5016–5031.

Gao S., Liu X., Yuan H., Hattendorf B., Günther D., Chen L. and Hu S. (2002) Determination of forty two major and trace elements in USGS and NIST SRM Glasses by Laser Ablation-

Inductively Coupled Plasma-Mass Spectrometry. *Geostandard. Newslett.* **26**, 181–196.

Ghiorso M. and Sack R. (1995) Chemical mass transfer in magmatic processes: IV. A revised and internally consistent thermodynamic model for the interpolation and extrapolation of liquid–solid equilibria in magmatic systems at elevated temperatures and pressures. *Contrib. Mineral. Petrol.* **119**, 197–212.

Hartmann W. and Barlow N. (2006) Nature of the Martian uplands: effect on Martian meteorite age distribution and secondary cratering. *Meteorit. Planet. Sci.* **41**(10), 1453–1467.

Harvey J. and Baxter E. (2009) An improved method for TIMS high precision neodymium isotope analysis of very small aliquots (1–10 ng). *Chem. Geol.* **258**, 251–257.

Ikeda Y. (2004) Petrology of the Yamato 980459 shergottite. *Antarct. Met. Res.* **17**, 35–54.

Jagoutz E. (1989) Sr and Nd isotopic systematics in ALHA 77005: age of shock metamorphism in shergottites and magmatic differentiation on Mars. *Geochim. Cosmochim. Acta* **53**, 2429–2441.

Jagoutz E. (1991) Chronology of SNC meteorites. *Space Sci. Rev.* **56**, 13–22.

Jambon A., Barrat J., Sautter V., Gillet P., Göpel C., Javoy M., Joron J. and Lesourd M. (2002) The basaltic shergottite Northwest Africa 856: petrology and chemistry. *Meteorit. Planet. Sci.* **37**, 1147–1164.

Jones J. (1986) A discussion of isotopic systematics and mineral zoning in the shergottites: evidence for a 180 m.y. igneous crystallization age. *Geochim. Cosmochim. Acta* **50**, 969–977.

Lapen T., Mahlen N., Johnson C. and Beard B. (2004) High precision Lu and Hf isotope analyses of both spiked and unspiked samples: a new approach. *Geochem. Geophys. Geosyst.* doi:10.1029/2003GC0000582.

Lapen T., Medaris L., Johnson C. and Beard B. (2005) Archean to Middle Proterozoic evolution of Baltica subcontinental lithosphere: evidence from combined Sm–Nd and Lu–Hf isotope analyses of the Sandvik ultramafic body, Norway. *Contrib. Mineral. Petrol.* **150**, 131–145.

Lapen T., Brandon A., Beard B., Peslier A., Lee C.-T. and Dalton H. (2008) Lu–Hf age and isotopic systematics of the olivine-phyric shergottite RBT-04262 and implications for the sources of the enriched shergottites. *Lunar Planet. Sci. XXXIX*. Lunar Planet. Inst., Houston. #2073 (abstr.).

Lapen T., Righter M., Brandon A., Beard B., Shafer J. and Irving A. (2009) Lu–Hf isotope systematics of NWA 4468 and NWA 2990: implications for the sources of shergottites. *Lunar Planet. Sci. XXXX*. Lunar Planet. Inst., Houston. #2376 (abstr.).

Lapen T., Righter M., Brandon A., Debaille V., Beard B., Shafer J. and Peslier A. (2010) A younger age for ALH 84001 and its geochemical link to shergottite sources in Mars. *Science* **328**, 347–351.

Ludwig K. R. (2003) *Isoplot/EX, Version 3.6.3: A Geochronological Toolkit for Microsoft Excel*. Berkeley Geochronological Center, Berkeley, CA.

Mahlen N., Beard B., Johnson C. and Lapen T. (2008) An investigation of dissolution methods for Lu–Hf and Sm–Nd isotope studies in zircon- and garnet-bearing whole-rock samples. *Geochem. Geophys. Geosyst.* **9**. doi:10.1029/2007GC001605.

McDonough W. and Sun S. (1995) The composition of the Earth. *Chem. Geol.* **120**, 223–253.

McKay G., Wagstaff J. and Yang S.-R. (1986) Clinopyroxene REE distribution coefficients for shergottites: the REE content of the Shergotty melt. *Geochim. Cosmochim. Acta* **50**, 927–937.

McSween H., Eisenhour D., Taylor L., Wadhwa M. and Crozaz G. (1996) QUE94201 shergottite: crystallization of a Martian basaltic magma. *Geochim. Cosmochim. Acta* **60**, 4563–4569.

Neukum G., Basilevsky A., Kneissl T., Chapman M., van Gasselt S., Michael G., Jaumann R., Hoffmann H. and Lanz J. (2010) The geologic evolution of Mars: episodicity of resurfacing events and ages from cratering analysis of image data and correlation with radiometric ages of Martian meteorites. *Earth Planet. Sci. Lett.* **294**, 204–222.

Nyquist L., Bogard D., Garrison D., Bansal B., Weismann H. and Shih C.-Y. (1991a) Thermal resetting of radiometric ages: I. Experimental investigation. *Lunar Planet. Sci. XXII*. Lunar Planet. Inst., Houston. #985–986 (abstr.).

Nyquist L., Bogard D., Garrison D., Bansal B., Weismann H. and Shih C.-Y. (1991b) Thermal resetting of radiometric ages: II. Modeling and applications. *Lunar Planet. Sci. XXII*. Lunar Planet. Inst., Houston. #987–988.

Nyquist L., Bogard D., Shih C.-Y., Reese Y. and Irving A. (2009) Concordant Rb–Sr, Sm–Nd, and Ar–Ar ages for Northwest Africa 1460: a 346 Ma old basaltic shergottite related to "lherzolitic" shergottites. *Geochim. Cosmochim. Acta* **73**, 4288–4309.

Paster T., Schauwecker D. and Haskin L. (1974) The behavior of some elements during solidification of the Skaergaard layered series. *Geochim. Cosmochim. Acta* **38**, 1549–1577.

Peslier A., Hnatyshin D., Herd C., Walton E., Brandon A., Shafer J. and Lapen T. (2010) Crystallization, melt inclusion, and redox history of a new Martian meteorite: olivine-phyric shergottite LAR 06319. *Geochim. Cosmochim. Acta* **74**, 4543–4576.

Rakovan J., McDaniel D. and Reeder R. (1997) Use of surface-controlled REE sectoral zoning in apatite from Llallagua, Bolivia, to determine a single crystal Sm–Nd age. *Earth Planet. Sci. Lett.* **146**, 329–336.

Rubin A., Warren P., Greenwood J., Verish R., Leshin L., Hervig R., Clayton R. and Mayeda T. (2000) Los Angeles: the most differentiated basaltic martian meteorite. *Geology* **28**, 1011–1014.

Rumble, III, D. and Irving A. (2009) Dispersion of oxygen isotopic compositions among 42 Martian meteorites determined by laser fluorination: evidence for assimilation of (ancient) altered crust. *Lunar Planet. Sci. XXXX*. Lunar Planet. Inst., Houston. #2293 (abstr.).

Salters V. and Stracke A. (2004) Compositions of the depleted mantle. *Geochem. Geophys. Geosyst.* **5**. doi:10.1029/2003GC000597.

Shih C.-Y., Nyquist L., Wiesmann H. and Barrat J. (2003) Age and petrogenesis of picritic shergottite NWA 1068: Sm–Nd and Rb–Sr isotopic studies. *Lunar Planet. Sci. XXXIV*. Lunar Planet. Inst., Houston. #1439 (abstr.).

Shih C.-Y., Nyquist L. and Reese Y. (2009) Rb–Sr and Sm–Nd studies of olivine-phyric shergottites RBT 04262 and LAR 06319: isotopic evidence for relationship to enriched basaltic shergottites. *Lunar Planet. Sci. XXXX*. Lunar Planet. Inst., Houston. #1360 (abstr.).

Snyder G., Taylor L. and Neal C. (1992) A chemical model for generating the sources of mare basalts: combined equilibrium and fractional crystallization of the lunar magmasphere. *Geochim. Cosmochim. Acta* **56**, 3809–3823.

Symes S., Borg L., Shearer C. and Irving A. (2008) The age of the martian meteorite Northwest Africa 1195 and the differentiation history of the shergottites. *Geochim. Cosmochim. Acta* **72**, 1696–1710.

Usui T., McSween H. and Floss C. (2008) Petrogenesis of olivine-phyric shergottite Yamato 980459, revisited. *Geochim. Cosmochim. Acta* **72**, 1711–1730.

Wadhwa M., McSween H. and Crozaz G. (1994) Petrogenesis of shergottite meteorites inferred from minor and trace

element microdistributions. *Geochim. Cosmochim. Acta* **58**, 4213–4229.

Walton E., Kelley S. and Herd C. (2008) Isotopic and petrographic evidence for young Martian basalts. *Geochim. Cosmochim. Acta* **72**, 5819–5837.

York D. (1966) Least squares fitting of a straight line. *Can. J. Phys.* **44**, 1079–1086.

Zindler A. and Jagoutz E. (1988) Mantle cryptology. *Geochim. Cosmochim. Acta* **52**, 319–333.

*Associate editor:* Richard J. Walker